https://dx.doi.org/10.21577/0103-5053.20210083

J. Braz. Chem. Soc., Vol. 32, No. 9, 1711-1738, 2021

Review

Interfacial Electron Transfer in Dye-Sensitized TiO_2 Devices for Solar Energy Conversion

Andressa V. Müller, *,[a] *Wendel M. Wierzba,*[a] *Mariana N. Pastorelli*[a] *and André S. Polo* *,[a]

[a]*Centro de Ciências Naturais e Humanas, Universidade Federal do ABC (UFABC), Av. dos Estados, 5001, 09210-580 Santo André-SP, Brazil*

The development of cost-effective molecular devices that efficiently capture and convert sunlight into other useful forms of energy is a promising approach to meet the world's increasing energy demands. These devices are designed through a successful combination of materials and molecules that work synergistically to promote light-driven chemical reactions. Light absorption by a surface-bound chromophore triggers a sequence of interfacial electron transfer processes. The efficiencies of the devices are governed by the dynamic balance between the electron transfer reactions that promote energy conversion and undesirable side reactions. Therefore, it is necessary to understand and control these processes to optimize the design of the components of the devices and to achieve higher energy conversion efficiencies. In this context, this review discusses general aspects of interfacial electron transfer reactions in dye-sensitized TiO_2 molecular devices for solar energy conversion. A theoretical background on the Marcus-Gerischer theory for interfacial electron transfer and theoretical models for electron transport within TiO_2 films are provided. An overview of dye-sensitized solar cells (DSSCs) and dye-sensitized photoelectrosynthesis cells (DSPECs) is presented, and the electron transfer and transport processes that occur in both classes of devices are emphasized and detailed. Finally, the main spectroscopic, electrochemical and photoelectrochemical experimental techniques that are employed to elucidate the kinetics of the electron transfer reactions discussed in this review are presented.

Keywords: electron transfer, solar energy conversion, dye-sensitized solar cells, artificial photosynthesis, dye-sensitized photoelectrosynthesis cells

1. Introduction

The search for clean, safe and sustainable energy sources is one of the most important scientific challenges in this century. In 2018, the global primary energy consumption was 6.0×10^{20} J, corresponding to an average consumption rate of 19 TW *per* year.[1] In the future, this value will certainly rise due to populational and economic growth. Based on current projections, the world's primary energy consumption rate will almost double (33 TW) in 2050 and reach 59 TW by 2100.[2] Solar energy is a renewable alternative that can meet these increasing global energy demands. The sun provides 4.3×10^{20} J of energy to the earth in one hour,[3] which is more than the energy currently consumed in eight months. It is estimated that photosynthesis alone produces more than 100 billion tons of dry biomass annually, corresponding to an average energy storage rate of 100 TW *per* year.[4] However, in 2018, fossil fuels still had 80% of the share of the total final energy consumption, and only 2.8% of electricity was provided by the sun.[5] A large gap exists between our present use of solar energy and its undeveloped potential. The development of new technologies to capture and convert sunlight in storable or usable ways that are cost-effective and highly efficient is imperative for the future of humankind.

In recent decades, a wide range of technologies based on molecular devices have been developed.[6-15] The main approaches are the direct conversion of light into electricity, for example, using dye-sensitized solar cells (DSSCs),[16-37] or its storage in chemical energy through light-driven water splitting[9,38-52] or carbon dioxide reduction[53-67] in systems for solar fuel production. These devices are comprised of a successful combination of materials and molecules that work synergistically to promote light-driven chemical reactions. At their cores, semiconductor metal oxide films are usually present. Mesoporous anatase titanium

*e-mail: andressa.muller@ufabc.edu.br; andre.polo@ufabc.edu.br

dioxide (TiO_2) is the most common material of choice due to its low cost, wide availability, nontoxicity and biocompatibility.[24,68] Mesoporous films are composed of a network of nanocrystalline particles that have been sintered together to allow electronic conduction to take place.[69] TiO_2 is a wide-bandgap semiconductor (E_g = 3.2 eV) that mainly absorbs ultraviolet radiation. It is important to note that more than 40% of sunlight is in the visible region; thus, TiO_2 must be sensitized to this region by molecular chromophores chemically bound to its surface to efficiently collect this energy, Figure 1a.[70,71] Typical mesoporous films, with porosity values of 50-60%, have surface areas available for dye chemisorption over a thousand times that of flat, unstructured electrodes of the same geometrical size;[23] thus, they are capable of high sunlight absorption.

After light absorption by the chromophore, it reaches an excited state, S*, from which it can transfer an electron to TiO_2, yielding a charge-separated state that consists of an electron injected into the metal oxide, $TiO_2(e^-)$, and an oxidized sensitizer molecule, S^+, as shown in Figure 1b. Sequentially, several different electron transfer reactions can take place in one or more interfaces between TiO_2, the surface-bound sensitizer and catalysts, and species present in the surrounding solvent/electrolyte, Figure 1c. Which specific electron transfer processes will succeed depends on the function, components and architecture of the device.[72-74] The devices are rationally designed to increase the efficiencies and rate constants of the interfacial electron transfer processes that promote solar energy conversion. However, undesirable electron transfer side reactions exist and may inhibit energy conversion. The dynamic balance between the forward and backward electron transfer reactions drives the energy conversion efficiency in these systems. The goal in most physical-chemical studies is to understand and quantify the rate constants of each individual electron transfer process to obtain guidelines to optimize the design of the components and achieve higher energy conversion efficiencies.

Envisioning the importance of understanding the interfacial electron transfer chemistry that takes place in dye-sensitized TiO_2 devices for solar energy conversion, in the context of the pursuit of further improvements to these devices through different approaches, such as molecular engineering, modifications of the materials, and fundamental investigations, the fundamentals of interfacial electron transfer in TiO_2 molecular devices for solar energy conversion are visited in this review. In the first two sections, the theoretical background of the Marcus-Gerischer theory for interfacial electron transfer and that of theoretical models for electron transport within TiO_2 films will be provided. Then, an overview focusing on dye-sensitized solar cells and dye-sensitized photoelectrosynthesis cells (DSPECs) will be presented, emphasizing and detailing the electron transfer and transport processes that occur in both classes of devices. Finally, the most common spectroscopic, electrochemical and photoelectrochemical characterization techniques that are employed to elucidate the kinetics of the electron transfer reactions in these systems will be overviewed.

2. Theoretical Basis for Interfacial Electron Transfer

The Marcus-Gerischer theory is the foundation for understanding the interfacial electron transfer dynamics

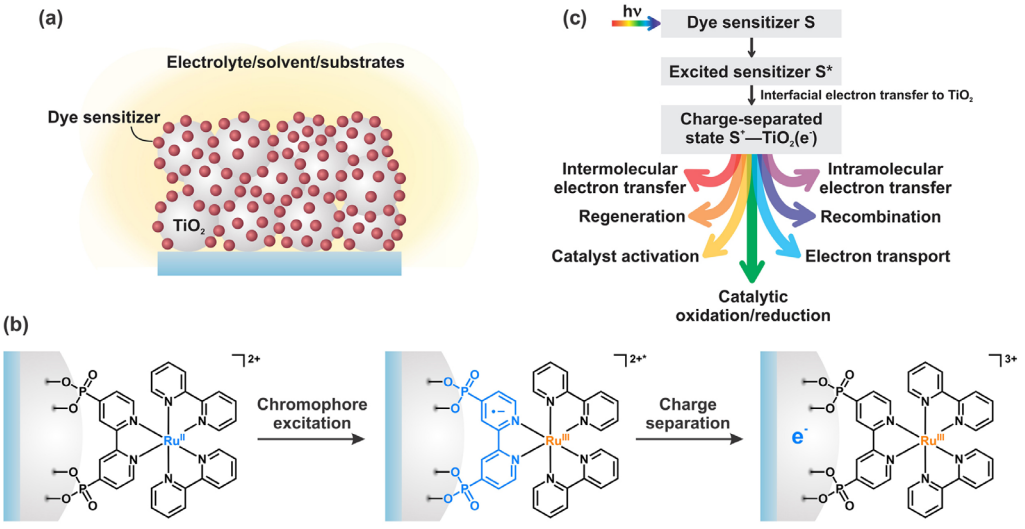

Figure 1. (a) General representation of a dye-sensitized TiO_2 film, (b) representation of the excitation of the chromophore and formation of a charge-separated state in a TiO_2 film sensitized by a ruthenium(II) dye, and (c) schematic representation of the working principles of a typical TiO_2 molecular device for solar energy conversion, featuring the excitation of the dye sensitizer, excited state electron injection into TiO_2 and some of the electron transfer reactions that may follow the charge-separation step.

occurring in molecular devices for solar energy conversion. This theory was initially developed by Rudolph Marcus for outer-sphere electron transfer reactions between donor and acceptor molecules in homogeneous solutions[75-83] and was further adapted and completed with the approaches developed by Heinz Gerischer to explain heterogeneous interfacial electron transfers occurring in interfaces.[84,85] These theories will be briefly presented in this section, with the aim to provide the reader with the basis to understand the various electron transfer processes that take place in dye-sensitized TiO_2 devices after light absorption.

2.1. Electron transfer in homogeneous solutions

Electron transfer from a donor to an acceptor is always accompanied by nuclear modifications of these species and of the surrounding medium. When the donor is oxidized and the acceptor is reduced, their electron densities change, naturally resulting in modifications to their bond lengths, angles, and vibrational modes, as well as their interaction with the surrounding solvent dipoles. However, following the Franck-Condon principle, the electron transfer step is instantaneous compared to the translational, rotational and vibrational nuclear motion of the reactants and the solvent. Therefore, in an electron transfer reaction, the nuclear configurations of all involved species must partially reorganize for the donor/acceptor reactants to achieve a transition state configuration before electron transfer, as shown in Figure 2. This nuclear reorganization is related to the activation energy $\Delta G^{\ddagger}$, which is an energetic barrier for the electron transfer process. After reaching the transition state, the electron transfer occurs quickly, with subsequent nuclear rearrangements occurring to accommodate the products.

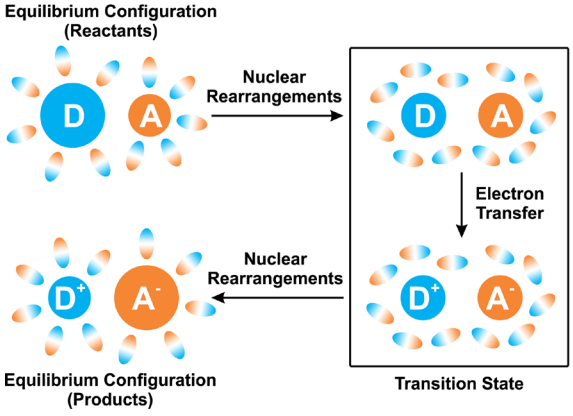

Figure 2. Representation of an electron transfer reaction between a donor (D) and an acceptor (A). The nuclear configurations of the reactants and of the surrounding medium must partially reorganize before the electron transfer occurs.

The energetics of an electron transfer can be represented by the reaction energy surfaces. In Marcus theory, the reactants and products are represented by two intersecting parabolas, each representing a harmonic oscillator comprised by the collective contributions of the spatial arrangement of the nuclei of the donor/acceptor species and the solvent, as shown in Figure 3. The surfaces are interpreted as increases in the Gibbs free energy (or potential energy) that result from bond distortions and changes in dipole orientations away from the equilibrium position.[86] The force constants of the harmonic oscillator are fixed for reactants and products and are directly related to the reorganization energy λ, which is defined as the energy necessary to distort the reactants from their equilibrium configuration to the equilibrium configuration of the products, without any electron transfer.[87]

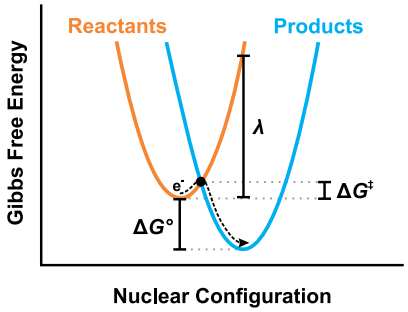

Figure 3. Reaction Gibbs free energy surfaces as a function of the nuclear configuration for a nonadiabatic electron transfer reaction. The dashed arrow represents the reaction pathway.

The electron transfer occurs at the intersection of the curves, where the energies of the reactant and product surfaces are equal (indicated by the black dot in Figure 3). At this point, equation 1 can be mathematically extracted and provides an explicit connection between the kinetics and thermodynamics of the electron transfer process.[88] The parabolic dependence of $\Delta G^{\ddagger}$ on the driving force $-\Delta G^{\circ}$ for the electron transfer results in different kinetic regimes, as shown in Figure 4. Isoergonic reactions ($\Delta G^{\circ} = 0$), in which $\Delta G^{\ddagger} = \lambda/4$, are denominated self-exchange reactions. The normal regime comprises weak exergonic reactions, i.e., $-\Delta G^{\circ} < \lambda$, in which the activation energy decreases with an increasing driving force. At $-\Delta G^{\circ} = \lambda$, the reaction becomes barrierless ($\Delta G^{\ddagger} = 0$), and a maximum rate constant is achieved. Any further increase in $-\Delta G^{\circ}$ leads to new increases in $\Delta G^{\ddagger}$ (inverted regime).

$$\Delta G^{\ddagger} = \frac{(\Delta G^{\circ} + \lambda)^2}{4\lambda} \quad (1)$$

From the transition state theory and equation 1, the relationship between electron transfer rate constants, k_{ET},

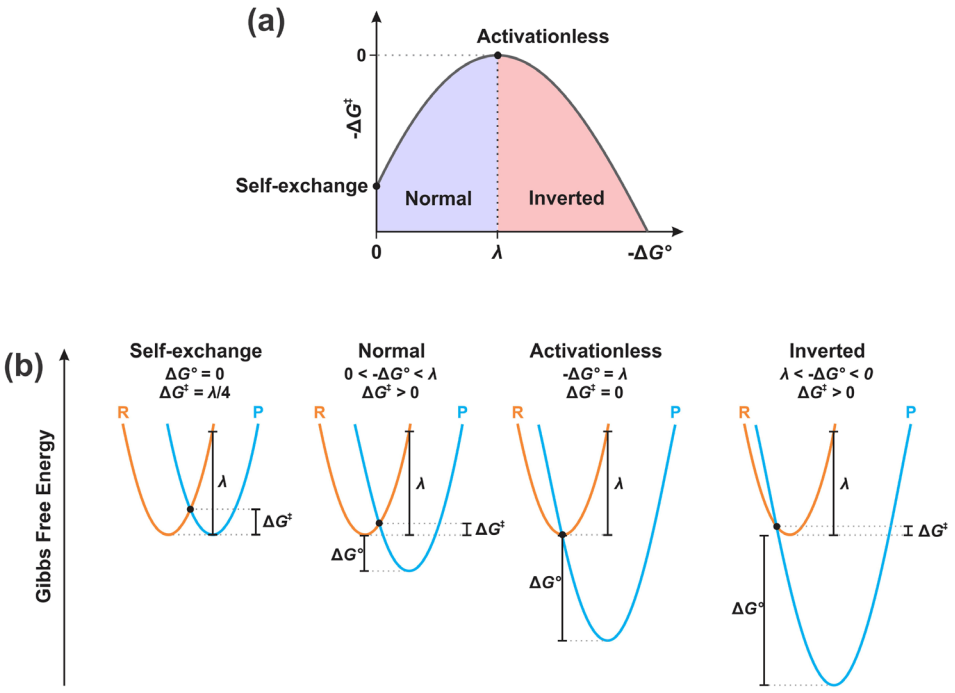

Figure 4. (a) Parabolic dependence of $-\Delta G^{\ddagger}$ on the driving force $-\Delta G^{\circ}$ for electron transfer and (b) schematic representation of free Gibbs energy surfaces along the nuclear configuration of a nonadiabatic electron transfer for four kinetic regimes: self-exchange reactions ($\Delta G^{\circ} = 0$), normal regime for weak exergonic reactions ($0 < -\Delta G^{\circ} < \lambda$), activationless reactions ($\Delta G^{\ddagger} = 0$ and $\Delta G^{\circ} = \lambda$), and inverted electron transfer for highly exergonic reactions ($\lambda < -\Delta G^{\circ} < 0$).

and activation free energy is given by equation 2, where k_B is the Boltzmann constant, T is the absolute temperature and A is a pre-exponential factor that depends on the frequency of crossing the energy barrier.

$$k_{ET} = A \exp\left(-\frac{(\Delta G^{\circ} + \lambda)^2}{4\lambda k_B T}\right) \quad (2)$$

The probability of crossing the energy barrier depends on the extent of the vibrational overlap between the reactant and product surfaces, Figure 5, and is referred to as electronic coupling, H_{DA}.[83] When H_{DA} is small, the electron transfer is referred to as nonadiabatic electron transfer. When the coupling is sufficiently large, the electron transfer is called

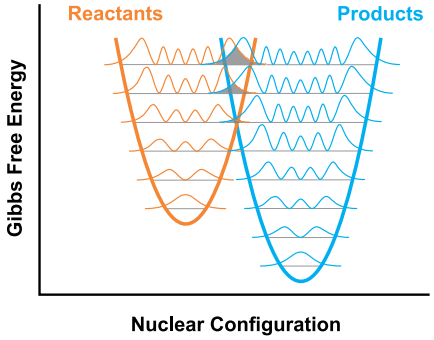

Figure 5. Schematic energy surfaces of the reactants and products and the vibronic overlap between them, which is represented by the gray regions (adapted from reference 83).

an adiabatic reaction.[86,89,90] For nonadiabatic and weakly adiabatic electron transfers, the semiclassical equation 3, where $\hbar$ is the reduced Planck constant, is valid to express the electron transfer rate constants. It completely characterizes the electron transfer reaction in terms of three quantities that can be determined experimentally but not independently, i.e., the driving force ΔG°, the reorganization energy λ and the electronic coupling H_{DA}.

$$k_{ET} = \frac{2\pi}{\hbar} \frac{|H_{DA}|^2}{\sqrt{4\pi\lambda k_B T}} \exp\left(-\frac{(\Delta G^{\circ} + \lambda)^2}{4\lambda k_B T}\right) \quad (3)$$

The electronic coupling usually decreases exponentially with increasing distance δ between the donor and acceptor, as described by equation 4, where β is the attenuation factor that captures the steepness of this decrease, and H_{DA}^{0} is the electronic coupling at van der Waals separation, δ_0.[18,91-93]

$$H_{DA} = H_{DA}^{0} \exp\left(-(\beta/2)(\delta - \delta_0)\right) \quad (4)$$

Although the general considerations of Marcus theory presented above are valid for interfacial electron transfer between TiO_2 and molecular species, there is a fundamental difference between homogeneous and heterogeneous systems. Unlike molecules that are treated as having discrete energy levels, TiO_2 is a semiconductor that has a broad continuum distribution of electronic

states that can participate in an electron transfer. The metal oxide cannot be treated as a single parabola, and a different approach is necessary to model a heterogeneous electron transfer.

2.2. Heterogeneous electron transfer-the Marcus-Gerischer approach

The Gerischer model uses a different framework to account for interfacial electron transfers occurring between semiconductor solids and molecular species.[94] Instead of relying on discrete energy levels, this model is based on the energy distributions of both the semiconductor and the molecules on its surface.

The distribution of the electronic states of the semiconductor is characterized by its density of states (DOS), that is, the number of states available to be occupied by the electrons at each level of energy. In the case of TiO_2, its valence band is comprised mainly of the overlap of the oxygen p-orbitals, and the conduction band is comprised mainly of unfilled Ti d-orbitals.[95,96] Their density of states has a parabolic dependence on the energy E. The DOS of the conduction band $g_c(E)$, for example, is given by equation 5, where m* is the electron effective mass and E_{CB} is the conduction band edge energy.[97]

$$g_c(E) = \frac{1}{2\pi^2\hbar^3}\left(2m^*\right)^{3/2}\left(E - E_{CB}\right)^{1/2} \quad (5)$$

Nanocrystalline TiO_2 films also exhibit electronic energy levels within the bandgap of the metal oxide. Such bandgap states are commonly referred to as trap states or localized states. They arise from defects in the crystal structure of TiO_2, such as Ti^{4+} sites[98,99] that result from oxygen vacancies,[100,101] adsorbed species on the film and/or intercalation of cations,[102,103] and can be localized in the bulk, grain boundaries or surface regions of the oxide.[104-108] The density and energetics of such traps are described by an exponentially decreasing tail of states below the conduction band, $g_t(E)$, equation 6, where N_L is the total density of traps, and T_0 is a parameter in temperature units that determines the depth of the distribution.[69,109,110] These traps directly influence the electron transport within the TiO_2 film and the energy loss mechanisms.

$$g_t(E) = \frac{N_L}{k_B T_0} e^{(E-E_{CB})/k_B T_0} \quad (6)$$

In the Gerischer model, the energy levels of the molecule involved in the electron transfer differ from the discrete thermodynamic standard redox potential $E°_{redox}$ and are also described by a distribution of electronic states based on the following microscopic description. The molecular species are surrounded by a specific solvation shell that is different for the donor (reduced) and acceptor (oxidized) species since their interactions with the solvent are different.[111,112] Thus, the energy states of the molecular species are split into two, as shown in the diagram in Figure 6a.

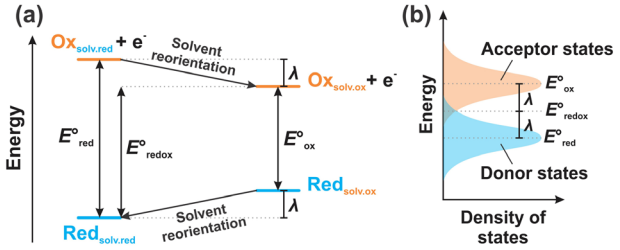

Figure 6. (a) Energy diagram for the oxidation or reduction of a solvated molecular species according to the Gerischer model and (b) the corresponding energy distributions (adapted from reference 87).

The energy of the molecular species in its reduced state is indicated by $Red_{solv.red}$. The subscript indicates that the solvation shell of the species is the equilibrium configuration for the reduced state. An energy $E°_{red}$ is required to transfer one electron from this reduced species to vacuum. Since the electron transfer is very fast in comparison to the reorganization of the solvent dipoles, the oxidized species formed has a solvation shell that is typical for the reduced species, $Ox_{solv.red}$. The solvent dipoles reorganize themselves after the electron transfer occurs until the oxidized species reach their equilibrium state, $Ox_{solv.ox}$. The energy that is involved in this relaxation process is the reorganization energy λ that was introduced for Marcus theory. The opposite electron transfer process occurs in a similar fashion; an $E°_{ox}$ difference in energy leads to the rapid formation of $Red_{solv.ox}$, followed by reorganization of the solvent.

The fluctuation in the solvent configurations around the reduced and oxidized species leads to a broadening of the electronic levels, as shown in Figure 6b, giving rise to Gaussian distributions of solvated energy states for the donor and acceptor species, $W_{red}(E)$ and $W_{ox}(E)$, respectively, as shown in equations 7 and 8.[111,113] The density of electronic states W(E) is proportional to the concentration of reduced or oxidized species at energy E.

$$W_{red}(E) = \frac{1}{\sqrt{4\pi\lambda k_B T}} \exp\left(-\frac{\left(E - E°_{redox} + \lambda\right)^2}{4\lambda k_B T}\right) \quad (7)$$

$$W_{ox}(E) = \frac{1}{\sqrt{4\pi\lambda k_B T}} \exp\left(-\frac{\left(E - E°_{redox} - \lambda\right)^2}{4\lambda k_B T}\right) \quad (8)$$

The electron transfer between the molecule and a semiconductor electrode occurs by the energetic overlap between their energy distributions. Depending on the relative energies, it can take place from an occupied state in the molecule to an acceptor state of the solid, as shown in Figure 7 for an excited state electron injection process, or from an occupied state in the semiconductor to an acceptor state in the molecule.

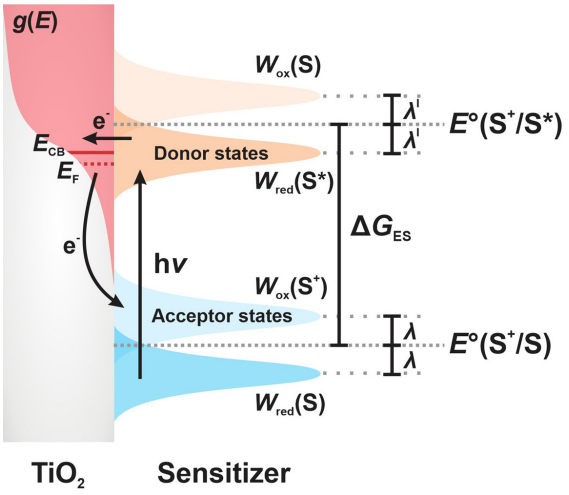

Figure 7. Schematic Gerischer diagram illustrating the interfacial electron injection from an excited sensitizer into the acceptor states of TiO_2 and subsequent back-electron transfer to the oxidized sensitizer (adapted from references 113-115).

In the framework of the energy distributions of the Gerischer model, the interfacial electron transfer rate constants follow the predictions of Marcus theory and can be mathematically described by equation 9, in which the occupation of electronic levels in the solid as a function of energy E is given by g(E)f(E,E_F), where g(E) is the total distribution of electronic levels, E_F is the Fermi level energy, and f(E,E_F) is the Fermi-Dirac function, which describes the probability of occupancy of the electronic levels, as shown in equation 10.[116-118] $H_{DA}(E)$ is the electronic coupling between the molecule and the solid. H_{DA} is often assumed to be constant across the whole density of states of the semiconductor.

$$k_{ET} = \frac{2\pi}{\hbar}\int_{-\infty}^{\infty} g(E)\, f(E,E_F)\left|H_{DA}(E)\right|^2 W(E)\, dE \qquad (9)$$

$$f(E,E_F) = \frac{1}{1+e^{(E-E_F)/k_BT}} \qquad (10)$$

Equation 9 predicts that the rate of interfacial electron transfer between the semiconductor and a molecular species on its surface is proportional to the overlap of occupied donor states with unoccupied acceptor states.[114] It also accurately predicts, for example, activationless electron injection from an excited sensitizer to acceptor states of the metal oxide when the excited state reduction potential of the sensitizer $E°(S^+/S^*)$ is greater than 2λ above E_{CB}, and slow back-electron transfer to the oxidized sensitizer when its ground state reduction potential $E°(S^+/S)$ lies within the forbidden energy gap of the semiconductor[70] (processes shown in Figure 7).

It is important to mention that other relevant theoretical models were also developed to describe the interfacial electron transfer reactions between semiconductors and molecules. Similar to the Marcus-Gerischer approach, the Sakata-Hashimoto-Hiramoto model[119,120] predicts that the electron transfer rate constants exhibit a direct dependence on the density of electronic states of the semiconductor and molecular species, and a quadratic dependence on the coupling between donor and acceptor energy levels. The Marcus-Gerischer and Sakata-Hashimoto-Hiramoto mathematical relationships are applicable for systems in which the interaction between the surface-bound molecule and the semiconductor is weak[121-123] (nonadiabatic processes), which is the case for most interfacial electron transfer reactions that occur between TiO_2 and molecular species.[124] However, if the interaction is strong, the electron transfer is generally described by the Creutz-Brunschwig-Sutin model.[125-127] In this case, direct electron transfer between the semiconductor and the surface-molecule can occur adiabatically during light excitation.[121-123] Electron transfer can take place between the highest occupied molecular orbitals (HOMO) of the molecule to the conduction band of the semiconductor (molecule-to-particle charge transfer), or from the valence band to the lowest unoccupied molecular orbitals (LUMO) of the molecule (particle-to-molecule charge transfer).

3. Electron Transport in Mesoporous TiO_2 Films

Electrons transferred from a surface-bound species to nanocrystalline TiO_2 films are transported through the material, and understanding the electron transport is fundamental to optimizing the efficiencies in solar energy conversion devices.[128-134]

When bulk, single-crystal TiO_2 is placed in contact with a liquid redox electrolyte, the energy states of the material surface are perturbed. Electrons are transferred across the semiconductor-electrolyte interface until the Fermi level of TiO_2 aligns with the redox potential of the electrolyte, forming a depletion layer at the TiO_2 surface relative to the bulk. As a consequence, an internal electric field is established within the semiconductor, inducing the migration of electrons within the material. However,

since the TiO_2 nanocrystallites used in solar energy conversion devices are small (typically 20 nm in diameter), the radius of the particle is smaller than the width of the depletion layer, and the electric field gradient in the film is negligible.[135-137] Electron migration can then be neglected, and the electron transport in nanocrystalline TiO_2 films can be described exclusively in terms of diffusion.[130,138]

A number of theoretical models have been developed to describe the diffusional electron transport occurring in nanocrystalline TiO_2. Although distinct, most of the models consider the electron transport in nanocrystalline TiO_2 films to be intrinsically dominated by the distribution of intraband gap states. The two main approaches are the multiple-trapping mechanism[104] and the hopping transport mechanism.[139]

Most studies investigating charge transport in TiO_2 solar energy conversion devices are interpreted in the framework of the multiple-trapping mechanism, as shown in Figure 8a. The foundation of the multiple-trapping mechanism is the existence of two electronic states in TiO_2 nanocrystalline films, which are the extended states (or conduction band states) that contain mobile electrons and the trap (or localized) states that are present below the conduction band edge. The model assumes that the electrons that are transferred to the TiO_2 film from a surface-bound molecular species are rapidly trapped in localized states. Then, they are thermally activated to the conduction band, where they move by diffusion until they are captured again by a trap state.

The multiple-trapping mechanism is extended through the following two approaches: the continuous-time random-walk (CTRW) model[130] and the random-flight model.[128] Both models propose that the electrons perform an independent random walk on a lattice of trap states. The central idea of the CTRW model is that each electron moves from a trap state to the conduction band after a waiting time. The waiting time depends only on the activation energy for detrapping from the trap state currently occupied. The electron then moves to a nearest-neighboring site in a random direction and adopts the waiting time of the new trap site, as shown in Figure 8b. The steps to all nearest neighbors are equally likely. The kinetics for charge transport are dominated by the time constants for release from the trap states.

Alternatively, the random-flight model included the possibility of many-neighbor interactions, as shown in Figure 8c. After an electron is thermally detrapped in the conduction band, it has an equal chance of being captured by any empty trap state within the TiO_2 nanocrystallite. Although similar to the nearest-neighbor CTRW model, the calculated trapping-detrapping rate as a function of time was many orders of magnitude slower.[114,138]

In the hopping transport mechanism, in contrast to the multiple-trapping framework, instead of detrapping electrons to the conduction band, electron transport occurs by direct tunneling between localized states in the band gap, as shown in Figure 8d. The upward and downward hopping rates between trap states depend on their energy difference and on the distance between the sites. The model predicts that the fastest upward hops occur predominantly towards sites in the vicinity of a specific level, i.e., the transport energy E_{tr}, independent of the energy of the starting site.

4. Overview of Interfacial Electron Transfer in Devices

In this section, the electron transfer reactions that govern the working principles of two classes of devices for solar energy conversion will be presented and discussed in terms of the models described in the previous sections. Dye-sensitized solar cells are photoelectrochemical devices for solar-to-electrical energy conversion, while dye-sensitized photoelectrosynthesis cells promote the conversion of solar energy to chemical energy stored in chemical substances. Although both devices exhibit several similarities, they present unique challenges concerning the control of the electron transfer reactions that promote and inhibit energy conversion.

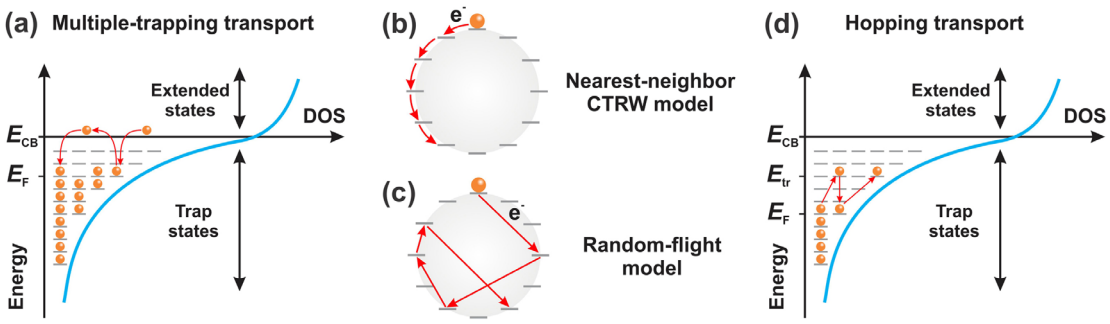

Figure 8. Schematic representation of (a) the multiple-trapping transport mechanism, the respective (b) nearest-neighbor continuous-time random walk and (c) random flight models, and (d) the hopping transport mechanism. The gray lines represent localized, trap states (adapted from references 138-140).

4.1. Dye-sensitized solar cells

Dye-sensitized solar cells (DSSCs) are regenerative photoelectrochemical devices capable of converting sunlight into electricity.[20,24,141] The materials employed for their construction are relatively cheap and common, and the devices can be prepared in a simple laboratory environment without strict demands on the purity of the materials.[19] DSSCs exhibit long-term durability, can use flexible substrates and are available in distinct colors, shapes, and transparency levels, thus allowing their incorporation into architectonic designs or different products.[22] Furthermore, their performance is better under diffuse light conditions and higher temperatures in comparison to other photovoltaic technologies.[26]

DSSCs are comprised of a dye-sensitized photoanode, a counterelectrode and a redox mediator in a sandwich arrangement, as shown in Figure 9a. The photoanode is the heart of the device, which is comprised of a mesoporous nanocrystalline semiconductor oxide film (typically TiO_2) that is deposited on the conductive surface of a transparent conductive glass (TCO) and is sensitized to visible light by inorganic,[16,21,115,142-147] organic[148-153] or natural[154-157] dyes adsorbed on its surface. The counterelectrode is another conductive glass covered by a thin layer of a catalyst, such as platinum or graphite.[158] Between these electrodes is placed a redox mediator that typically consists of a redox couple in an organic solvent.[159]

The DSSC is a good example of an energy conversion device in which its functioning depends on the dynamic competition between the interfacial electron transfer that arises from the complex interactions between its components, as shown in Figure 9b. This chemical complexity, however, must be unraveled and understood to guide the molecular and material design towards more efficient devices. The common strategy is to increase the rate constants of the forward electron transfer processes to promote energy conversion and inhibit competitive energy loss pathways.

4.1.1. Electron injection and excited state decay

The energy conversion process is initiated by the photoexcitation of the sensitizer, as shown in process (1) in Figure 9. From its excited state, the dye may inject an electron into the metal oxide acceptor states, generating a charge-separated state in which an electron resides in the TiO_2 nanoparticle and the oxidized dye remains on the surface.[160] The electron injection dynamics are often found to be biphasic.[161,162] The faster component is attributed to a "hot" electron injection from the unthermalized, high vibronic excited states of the sensitizer, i.e., process (2), that competes with vibrational relaxation, i.e., process (3). The slower component corresponds to the electron injection from the thermalized excited states of the sensitizer, i.e., process (4). To efficiently promote energy conversion, the electron injection components must be faster than the relaxation pathways to the ground state, i.e., process (5), which is characterized by the excited state lifetime of the dye. The injection efficiency (Φ_{inj}) can be determined from the injection (k_{inj}) and relaxation (k_{rlx}) rates given by equation 11.

$$\Phi_{inj} = \frac{k_{inj}}{k_{inj} + k_{rlx}} \quad (11)$$

According to the Marcus-Gerischer model for interfacial electron transfer, the electron injection rates depend on the overlap of the molecular donor levels with the acceptor states of the semiconductor. Upon raising the energy of the excited state of the dye, the injection rate is expected

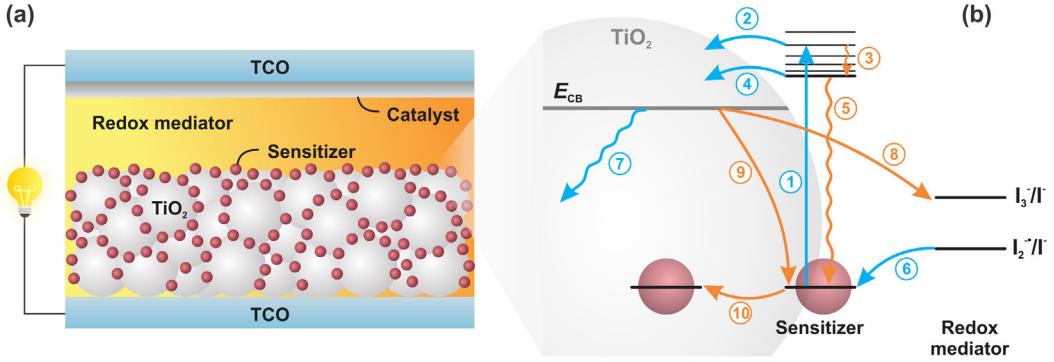

Figure 9. (a) Schematic representation of the arrangement of the components of a dye-sensitized solar cell. (b) Overview of the electron transfer and transport processes in a DSSC with an I^-/I_3^- redox mediator: (1) photoexcitation (< 10^{-15} s), (2) hot electron injection (10^{-13} to 10^{-12} s), (3) thermalization (10^{-13} to 10^{-12} s), (4) thermalized electron injection (10^{-12} to 10^{-10} s), (5) thermal relaxation to the ground state (10^{-9} to 10^{-8} s), (6) regeneration of the oxidized dye (10^{-9} to 10^{-6} s), (7) electron transport through the TiO_2 film (10^{-3} to 10^{-2} s), (8) recombination with acceptor species in the mediator (10^{-3} to 10^{0} s), (9) back-electron transfer (10^{-6} to 10^{-3} s), and (10) lateral intermolecular self-exchange (10^{-8} to 10^{-6} s). The blue arrows represent the processes that promote energy conversion, while the processes that inhibit energy conversion are represented by orange arrows (adapted from reference 19).

to increase due to the higher density of acceptor states in the metal oxide.[163] Sensitization by dyes with anchoring groups that promote efficient electronic coupling is another strategy to increase the injection rates and efficiency.[164-168]

4.1.2. Regeneration of the oxidized sensitizer

The regeneration of the oxidized dye occurs by electron transfer from the electron donor (reduced) species of the redox mediator, i.e., process (6). The best electrolyte to date is a solution of the I_3^-/I^- redox pair in nitriles.[159] The maximum voltage built by the DSSC is set by the energy difference between the Fermi level of the oxide and the standard reduction potential of the redox couple of the mediator. The two-electron reduction given by equation 12 is responsible for determining the maximum voltage achievable by the cell, but it is not directly responsible for regeneration. Instead, the $I_2^{-\bullet}/I^-$ couple seems to be responsible for reducing the oxidized dye.

$$I_3^- + 2e^- \rightarrow 3I^- \quad (12)$$

The pathway for the regeneration of the oxidized dye (S^+) by iodide is given by equations 13 to 15. The electron transfer from iodide to S^+ occurs under the formation of a ($S\cdots I$) complex.[169] The complex dissociates in the presence of a second iodide ion, forming the dye in its ground state and $I_2^{-\bullet}$. Two diiodide radicals dissociate into triiodide and iodide.

$$S^+ + I^- \rightarrow (S\cdots I) \quad (13)$$
$$(S\cdots I) + I^- \rightarrow S + I_2^{-\bullet} \quad (14)$$
$$2I_2^{-\bullet} \rightarrow I_3^- + I^- \quad (15)$$

The most straightforward strategy to accelerate the regeneration rate constants, k_{reg}, is to modulate the standard reduction potential of the sensitizer, increasing the driving force for electron transfer, as predicted by the Marcus homogeneous electron transfer theory in the normal region.[17,169-172]

4.1.3. Electron transport and reduction of acceptors at the counter electrode

The electrons that were injected into the metal oxide are transported through the mesoporous network, i.e., process (7), as proposed by the models described in section 3, and reach the back contact of the photoanode. The extracted charge flows by the external circuit, performing useful electrical work. The electrons then reach the counter electrode, where they reduce the oxidized species of the mediator by a catalyzed reaction, completing the circuit and returning the system to its initial state.

4.1.4. Electron recombination with acceptor species

During transport through the mesoporous film, the photoinjected electrons are within only a few nanometers of the oxidelelectrolyte interface.[69] Recombination of these electrons to acceptors in the electrolyte, i.e., process (8), or to the oxidized dye molecules, i.e., process (9), is a possibility that may prevent the injected electrons from being collected and may inhibit the overall energy conversion process. The competition between the rates of transport (k_{tr}) and recombination processes (k_{rec}) defines the charge collection efficiency (Φ_{col}), as given by equation 16, and ultimately the efficiency of the DSSCs.

$$\Phi_{col} = \frac{k_{tr}}{k_{tr} + k_{rec}} \quad (16)$$

The recombination of electrons in TiO_2 with the triiodide of the redox mediator is an important loss reaction. The mechanism for this recombination reaction is believed to be dominated by the multiple trapping of electrons.[173,174] The central idea is that after a number of detrapping events, the electrons may reach a surface trap state adjacent to the acceptor species and recombine by an interfacial electron transfer reaction.[138,175] The kinetics are rate-limited by the detrapping step.[114] It has been shown that modifying the structure of the dye sensitizer with long chains or bulky aromatic substituents reduces the rates of electron recombination to the acceptors in the mediator, most likely by inhibiting the access of electrolyte ions to the TiO_2 surface.[18,176]

Because the electrolyte permeates through the mesoporous oxide film all the way to the TCO substrate, a second recombination pathway is the recombination of electrons to triiodide from the part of the TCO substrate that is exposed to the electrolyte (not shown in Figure 9). This route is usually less important and can be easily suppressed by using a compact blocking layer of the metal oxide.[177-181]

The back-electron transfer to the oxidized dye molecules at the TiO_2 surface is a relevant recombination reaction, especially when the solar cell is under intense illumination (typical working conditions). Under these conditions, the concentration of photoinjected electrons in TiO_2 increases, and recombination becomes faster.

This electron transfer reaction is also modeled using the framework of multiple-trapping mechanisms previously discussed.[128,130,131,138] However, back-electron transfer reaction rates, k_{bet}, are not limited only by the transport of injected electrons.[182] After electron injection into the TiO_2 acceptor states, the surface-immobilized oxidized sensitizer can be translated away from the injection site through lateral intermolecular self-exchange reactions, i.e.,

process (10), without a loss of free energy. This process is commonly referred to as hole hopping and can be modeled by the Marcus theory for nonadiabatic electron transfer.[91,183] Rapid hole hopping promotes the formation of an encounter complex between the injected electron and the oxidized dye sensitizer prior to charge recombination, resulting in larger k_{bet} rate constants.[184] Therefore, both the electron transport and hole hopping govern the back-electron transfer kinetics.

Suppressing the back-electron transfer reaction to the oxidized molecules at the TiO_2 surface is a goal to increase the light-to-electrical energy conversion efficiency since recombination with the oxidized dye molecules competes directly with the regeneration process. In efficient devices, the regeneration efficiency (Φ_{reg}), as given by equation 17, must be close to unity.

$$\Phi_{reg} = \frac{k_{reg}}{k_{reg} + k_{rec}} \quad (17)$$

Strategies to inhibit this undesired recombination pathway include the design of new dye sensitizers that exhibit low electronic coupling for the self-exchange reaction, slowing down the hole-hopping process,[17,18] or modulating their energetics so that back-electron transfer occurs in the inverted Marcus region.[172,185]

4.2. Dye-sensitized photoelectrosynthesis cells

Although direct solar-to-electrical energy conversion is a possible alternative to supply the global energy consumption, the sun is an intermittent source that provides approximately only 6 h of useful energy *per* day on average.[186] For solar energy to become a primary energy source, it will have to be integrated with large-scale energy storage for power consumption at night or on cloudy days. A practical approach to address this issue is the direct conversion of solar energy into fuels.[41,187]

The inspiration for systems that store solar energy as fuels comes from a process that has been occurring in nature for 2.4 billion years, i.e., photosynthesis. Green plants and other photosynthetic organisms absorb photons, leading to sequential electron transfer reactions that promote the conversion of water and carbon dioxide into products with high-energy content stored in their chemical bonds, as given by equation 18.

$$6H_2O + 6CO_2 + 48h\upsilon \rightarrow C_6H_{12}O_6 + 6O_2 \quad (18)$$

The goal of artificial photosynthetic systems is to mimic these features to produce solar fuels using cheap substrates with low energy content but with higher efficiencies and a simpler design.[188] One of the main strategies is the photocatalytic production of hydrogen from water splitting,[189-196] as given by equations 19 and 20. The corresponding standard electrochemical reduction potentials E° are indicated *versus* normal hydrogen electrode (NHE).

$$2H_2O \rightarrow O_2 + 4e^- + 4H^+$$
$$E° = +1.23 - 0.059\ (pH)\ V\ vs.\ NHE \quad (19)$$
$$2H^+ + 2e^- \rightarrow H_2$$
$$E° = 0.00 - 0.059\ (pH)\ V\ vs.\ NHE \quad (20)$$

Another approach is to promote the light-driven reduction of CO_2 to yield CO, hydrocarbons, or other oxygenated carbon products, as given by equations 21 to 25.[56,197-202] As fuels, these products resulting from water splitting and CO_2 reduction are fully compatible with existing technologies for energy utilization and storage.[41]

$$CO_2 + 2H^+ + 2e^- \rightarrow CO + H_2O$$
$$E° = -0.52\ V\ vs.\ NHE\ (at\ pH\ 7) \quad (21)$$
$$CO_2 + 2H^+ + 2e^- \rightarrow HCOOH$$
$$E° = -0.61\ V\ vs.\ NHE\ (at\ pH\ 7) \quad (22)$$
$$CO_2 + 4H^+ + 4e^- \rightarrow HCHO + H_2O$$
$$E° = -0.48\ V\ vs.\ NHE\ (at\ pH\ 7) \quad (23)$$
$$CO_2 + 6H^+ + 6e^- \rightarrow CH_3OH + H_2O$$
$$E° = -0.38\ V\ vs.\ NHE\ (at\ pH\ 7) \quad (24)$$
$$CO_2 + 8H^+ + 8e^- \rightarrow CH_4 + 2H_2O$$
$$E° = -0.24\ V\ vs.\ NHE\ (at\ pH\ 7) \quad (25)$$

The main challenge to generate solar fuels is the need to integrate the absorption of several photons with multiple electron transfer events and the accumulation of charges that are required to drive the half-reactions given in equations 19 to 25.[203] The transfer of at least two electrons is necessary to generate carbon-reduced products, and four electrons are needed to drive water oxidation.[204] Dye-sensitized photoelectrosynthesis cells (DSPECs) are a promising approach to overcome this challenge. DSPECs combine the properties of nanocrystalline metal oxide semiconductors, molecular chromophores and catalysts in an integrated device.[12]

In DSPECs, solar fuel production is split into two different half-reactions at spatially separated electrodes. Figure 10 presents an example of a DSPEC scheme for water splitting, but there are other possibilities for different processes.[205-208] Oxidative chemistry occurs at the photoanode, and reduction takes place at the cathode.[48] The electrodes are in separate compartments to avoid the mixing of the products. The external circuit provides electronic connections between the isolated half-reactions, while

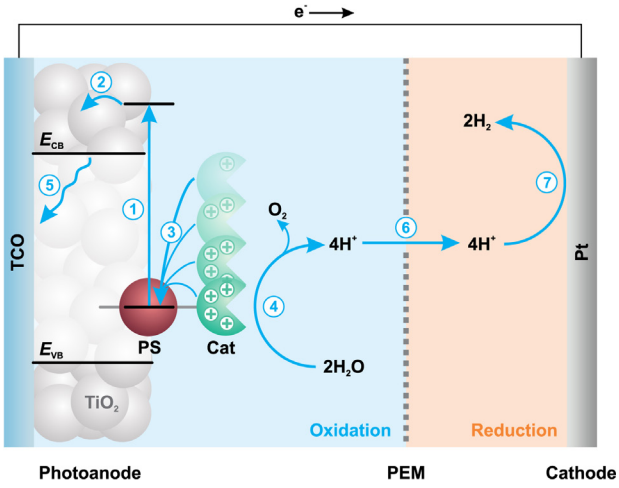

Figure 10. Schematic representation of a DSPEC for water oxidation and hydrogen production. The following processes are illustrated: (1) sequential photon excitation (< 10^{-15} s), (2) excited state electron injection (10^{-13} to 10^{-10} s), (3) sequential electron transfer events from the catalyst to the photosensitizer (catalyst activation) (10^{-12} to 10^{-6} s), (4) water oxidation (10^{-1} to 10^{1} s), (5) electron transport through the TiO_2 mesoporous film (10^{-3} to 10^{-2} s), (6) proton transfer to the cathode compartment, and (7) catalytic reduction of protons to H_2. PS is the photosensitizer, cat is the catalyst, and PEM is a proton exchange membrane (adapted from reference 41).

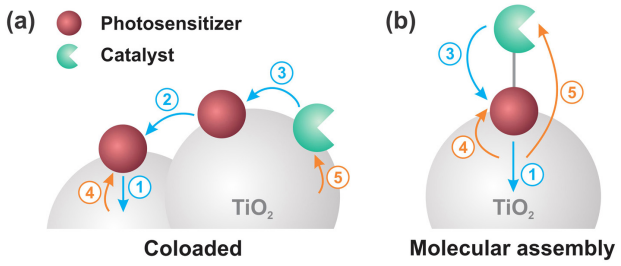

Figure 11. Representation of electron transfer processes in DSPEC photoanodes where the photosensitizer and catalyst are coloaded (a) or covalently linked in a molecular assembly (b). The following processes are illustrated: (1) excited state electron injection (10^{-13} to 10^{-10} s), (2) lateral intermolecular self-exchange (10^{-6} to 10^{-3} s), (3) electron transfer from the catalyst to the photosensitizer (catalyst activation) (10^{-12} to 10^{-6} s), (4) back-electron transfer (10^{-7} to 10^{-3} s), and (5) recombination to the activated catalyst (10^{-7} to 10^{-3} s). The blue arrows represent the forward electron transfer processes, and the orange arrows represent processes that inhibit energy conversion.

a proton exchange membrane allows protons to diffuse between the compartments.[187]

In a water splitting DSPEC, the photoanode is comprised of a mesoporous nanocrystalline n-type metal oxide semiconductor film, which is typically TiO_2, a molecular photosensitizer for light harvesting, and a catalytic center that drives the oxidation of substrates. Upon illumination, the chromophore absorbs light and is promoted to an excited state, from which it can transfer an electron to the metal oxide acceptor states, resulting in a charge-separated state that consists of an oxidized chromophore and an electron in TiO_2.[209,210] The injection process may have contributions from both the unthermalized and thermalized excited states of the chromophore[12] and is in competition with other excited state processes, such as thermal relaxation to the ground state or photoluminescence.[41] The kinetics and efficiency of electron injection depend on the coupling between the excited chromophore (donor states) and the distribution of acceptor states of TiO_2,[188] following the predictions of the Marcus-Gerischer model.

Injection is followed by activation of the water oxidation catalyst (i.e., formation of the oxidized forms of the catalyst) by the oxidized chromophore,[211] and the pathway depends on the strategy for combining both species. The photosensitizer and the catalyst may be separate species coadsorbed on the surface of the oxide or chemically linked in molecular assemblies, as shown in Figure 11.[195,212,213] In the first case, the oxidized chromophore is translated away from the injection site through lateral self-exchange reactions between neighboring sensitizers until it is reduced by an adjacent catalyst, beginning the catalyst activation.[188,209,214] In the case of molecular assemblies, oxidation of the catalyst occurs by intramolecular electron transfer to the oxidized chromophore. In this design, electron transfer is usually more rapid and efficient due to the close proximity of the donor and acceptor species.[12,195]

To drive water oxidation at the photoanode, the excitation-injection-activation cycle must be repeated four times sequentially to allow the stepwise accumulation of the multiple oxidative equivalents in the catalyst. However, the standard potentials for each successive oxidation usually show a significant difference due to the charge buildup in the highly oxidized states of the catalyst, and the activation becomes thermodynamically less favorable after each step.[188] A strategy to overcome this challenge is to design a catalyst that undergoes a proton-coupled electron transfer (PCET), where the electron transfer is accompanied by a proton transfer event, thus compensating for the localization of charges. It prevents the increase in charge buildup at the catalyst, allowing multiple oxidative equivalents to accumulate at a single catalytic site.[215,216]

After catalytic oxidation of the substrate by the fully activated catalyst, the molecular species bound to the semiconductor surface on the photoanode return to their initial states. The electrons that were injected by the photosensitizers into the acceptor states of TiO_2 are transported to the TCO back-contact by trapping/detrapping events.[217] In the aqueous environment of DSPECs, transport has a more complicated picture than presented in section 3. Protons intercalate into the TiO_2 lattice to compensate for the charge carriers, stabilizing the defect sites and leading to the formation of long-lived trap states that retard transport.[214,218,219] The electrons

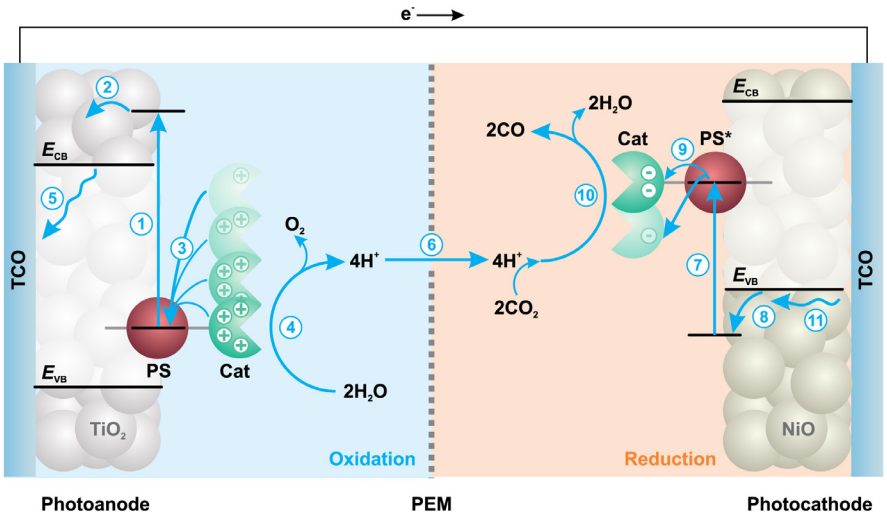

Figure 12. Schematic representation of a tandem DSPEC for the reduction of CO_2 to CO. The following processes are illustrated at the photoanode: (1) sequential photon excitation (< 10^{-15} s), (2) excited state electron injection (10^{-13} to 10^{-10} s), (3) sequential electron transfer events from the catalyst to the photosensitizer (catalyst activation) (10^{-12} to 10^{-6} s), (4) water oxidation (10^{-1} to 10^{1} s), (5) electron transport through the TiO_2 mesoporous film (10^{-3} to 10^{-2} s), and (6) proton transfer to the cathode compartment. At the photocathode, the following processes are illustrated: (7) sequential photon excitation (< 10^{-15} s), (8) excited state electron transfer (10^{-13} to 10^{-10} s), (9) sequential electron transfer events from the photosensitizer to the catalyst (catalyst activation) (10^{-12} to 10^{-6} s), (10) CO_2 reduction (10^{-1} to 10^{1} s), and (11) electron transport through the NiO film (10^{-2} to 1 s). PS is the photosensitizer, cat is the catalyst, and PEM is a proton exchange membrane (adapted from reference 41).

that reach the TCO back-contact are then delivered to the cathode, where in a dark catalytic reaction, protons are reduced to H_2. The protons necessary to drive the reduction reaction are provided by water oxidation at the photoanode.

An alternative design of DSPECs employs a photoactive cathode, forming a tandem device with a higher potential efficiency than for a single light-absorber system, as shown in Figure 12.[188,220] Tandem DSPECs are a promising configuration to promote CO_2 reduction using water as the electron source. The photocathodes in tandem DSPECs are typically comprised of p-type metal oxide semiconductor films (usually NiO)[221] sensitized by a molecular chromophore and a reduction catalyst.[222,223] As in the photoanode, the photosensitizer and catalyst may be coadsorbed on the metal oxide surface,[224] or they can be covalently linked in a molecular assembly.[221]

In the photocathode, the electron transfer pathway is the opposite of that of the photoanode. The photosensitizer is excited and transfers a hole to the valence band of the semiconductor (which means that an electron is transferred from the valence band of the metal oxide to the excited chromophore). The reduced photosensitizer transfers one electron to the catalyst, thus beginning its activation. The excitation-electron transfer cycle is repeated to accumulate enough reducing equivalents in the catalyst, which then promotes the photoreduction of the substrate.[41]

The performances of the different architectures of DSPECs are strongly dependent on the kinetics of the interfacial electron transfer events. The rates and efficiency of electron transfer between the chromophore and the semiconductor, lateral self-exchange, charge carrier transport, catalyst activation and the catalysis itself dictate the efficiency of the the solar fuel half-reactions.[217] In addition, the efficiencies of the devices are compromised due to undesirable electron transfer side reactions. The transport of electrons through the TiO_2 film to the back contact of the photoanode competes directly with recombination reactions, as previously shown in Figure 11. The injected electrons can undergo back-electron transfer to the oxidized sensitizer molecules, and the photogenerated redox equivalent is lost as heat to the surroundings.[195] Furthermore, the injected electrons can be scavenged by the oxidized catalyst at every step of its activation.[203] Both recombination pathways are controlled by the density of electrons in the film and the slow diffusional electron transport dynamics within TiO_2. These deleterious reactions can be partially suppressed by employing the molecular assembly approach. The proximity between the chromophore and the catalyst allows fast regeneration of the photosensitizer by the catalyst while translating the oxidative equivalents away from the TiO_2 surface. Another alternative is to increase the rate of catalysis, stabilizing the catalyst against side reactions.[217]

The problem of recombination reactions is particularly large for photocathodes since interfacial recombination is intrinsically much faster using NiO than with TiO_2.[188] Suppressing the interfacial recombination reactions in

the photocathode is essential to match the rates of water oxidation and fuel production to balance the need for reducing equivalents.

To achieve the goal of efficient solar fuel generation, it is necessary to understand and control all aspects of the multiple electron transfer events in DSPECs, especially regarding minimizing the unproductive electron transfer pathways. This requires a detailed kinetic investigation of each individual process.

5. Techniques for Characterization of Interfacial Electron Transfer

Characterization of the interfacial electron transfer reaction kinetics that occur in DSSCs, DSPECs, and other systems and devices for solar energy harnessing is the key to comprehending the effects of modifications of the individual components on their efficiency. Understanding the fundamental research regarding interfacial electron transfer is a necessary step to guide further improvements in molecular devices for solar energy conversion. Several spectroscopic, electrochemical and photoelectrochemical techniques are available to measure the electron transfer and transport rate constants over a wide range of timescales. Depending on the technique and the experimental conditions, these processes can be investigated independently or concomitantly in complete operating devices. When combined, these techniques may provide a complete picture of the electron transfer dynamics in devices, allowing us to understand the fundamental aspects that govern the energy conversion processes in these systems. In this section, different experimental techniques employed to investigate electron transfer dynamics in dye-sensitized TiO_2 devices for solar energy conversion will be overviewed. Selected examples will be discussed to illustrate how these techniques can be applied to solve problems related to electron transfer in DSSCs and DSPECs.

5.1. Pulsed laser spectroscopy techniques

Spectroscopic techniques that use a pulsed laser are widely employed to investigate the interfacial electron transfer chemistry within dye-sensitized TiO_2 devices for energy conversion, yielding information on photoinduced electron transfer rates, intermediate states, and products of photoinitiated reactions. Pulsed laser techniques are based on the excitation of the surface-bound chromophore by a short UV-Vis laser pulse (also called a pump pulse) and tracking the light-induced changes in the sample over time. These changes may be probed by measuring the time profile of the emission from the sample (time-resolved photoluminescence spectroscopy) or by monitoring the absorption of a second light beam (the probe beam) by the sample as a function of time. In transient absorption spectroscopy (TAS, section 5.1.1), the probe beam is in the UV-Vis region,[225,226] while in time-resolved infrared spectroscopy (TRIR, section 5.1.2), the probe beam is in the infrared region.[227] Due to their versatility and robustness, TAS and TRIR are probably the most commonly used pulsed laser techniques to study photoinduced processes in TiO_2 molecular devices, and they will be detailed below.

In both TAS and TRIR, the changes in the sample absorbance are recorded as a function of time for a given probe wavelength, as shown in Figure 13a. The changes in the absorbance $\Delta A(\lambda,t)$ are calculated from the ratio between the intensity (I) of the transmitted probe beam in the presence and the absence of the pump light, according to equation 26.[225,226] The complete transient spectrum is built by repeating the measurements at various probe wavelengths and is represented for a given time delay, as shown in Figure 13b.

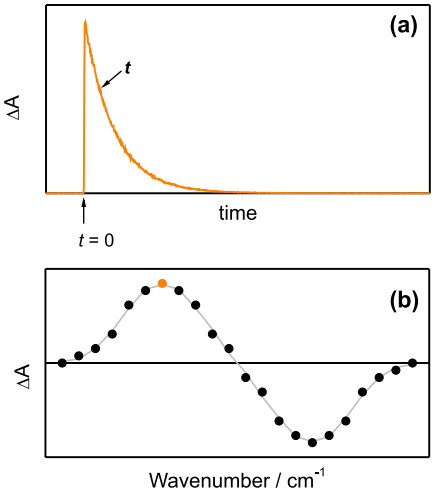

Figure 13. (a) Time evolution of the changes in the IR absorbance at a given probe wavelength, and (b) the TRIR transient spectra for a given time delay t after the pump flash. The orange dot is the ΔA determined for the time delay t at the probe wavenumber where the kinetic curve (a) was measured.

$$\Delta A(\lambda,t) = -\log\left(\frac{I(\lambda,t)_{pumped}}{I(\lambda,t)_{unpumped}}\right) \quad (26)$$

The changes in absorbance over time arise from differences in the steady-state UV-Vis or IR absorption spectra and the time profiles of the species that are formed and/or consumed after light excitation, as shown in Figure 14. As a fraction of the chromophore is promoted to the excited state by the pump pulse, the ground state is depopulated. Consequently, the ground-state absorption in the excited sample decreases, and a negative signal (bleach) is observed in the ΔA spectrum. The excited chromophore

may absorb light from the probe beam, resulting in a positive signal in the ΔA spectrum. Furthermore, positive signals in the ΔA spectrum may arise due to light absorption by products formed in the light-induced electron transfer reactions, such as oxidized or reduced chromophores and catalysts, as well as of electrons in TiO_2, oxidized species in the redox electrolyte, or other short-lived intermediates and products. In the case of UV-Vis TAS, stimulated emission from the chromophore's excited state back to the ground state and the Stark effect[228-230] may additionally contribute to the transient spectrum.

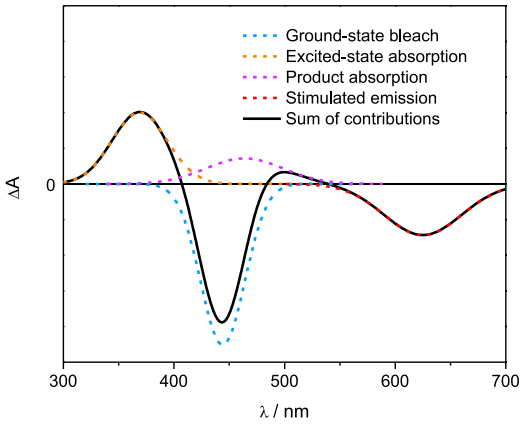

Figure 14. Representation of the contributions to a ΔA transient absorption spectrum at a given time delay. Each individual contribution (dashed lines) is time-dependent, and the overall spectral sum (solid line) varies as a function of time after excitation.

The technique and experimental conditions chosen will define which interfacial electron processes and transient species are observed, but it ultimately depends on the timescale of the experiment. Thus, the instruments can be assembled in various optical configurations spanning a wide range of time resolutions.

Fast pulsed laser techniques, as shown in Figure 15a, measure spectral changes from nanoseconds to milliseconds. In a typical instrumental setup, the pump pulse that excites the sample is generated by a nanosecond laser (Nd:YAG or nitrogen lasers). The probe beam is generated separately by a continuous white (TAS) or infrared (TRIR) light source. The sample, which is commonly a sensitized film immersed in a solvent,[17,18] is placed between the pump and probe beams. The changes in the absorption of the probe beam are monitored as a function of time using a suitable fast electronic detector, resulting in a kinetic trace at the selected probe wavelength. The experiment can be repeated at various probe wavelengths, yielding the transient spectrum, as shown in Figure 13b.[66,231] Typical experimental setups of TAS and TRIR may differ regarding whether the wavelength of the probe beam is selected before (TRIR) or after (TAS) passing through the sample.

In the case of fast TRIR, an alternative setup offers the advantage of allowing us to probe a large range of IR frequencies simultaneously. This technique is known as step-scan TRIR. This setup involves a movable mirror in a Michelson interferometer being displaced in a stepwise manner. For each stop position of the mirror, the changes in IR absorption that follow the pump excitation are measured, resulting in time-dependent interferograms. The Fourier transformation of the interferograms of the complete set of stop positions of the mirror at a particular time delay yields the corresponding difference infrared absorption spectrum.[231-233]

In contrast to fast techniques, ultrafast pulsed laser setups, as shown in Figure 15b, are employed to investigate processes that occur from femtoseconds to a few nanoseconds after light excitation. In ultrafast setups, the probe beam is not continuous but is a pulse. The subnanosecond time resolution TRIR is achieved by delaying the probe pulse with respect to the pump pulse, as shown in Figure 16, both generated from the same femtosecond laser (Ti:sapphire).

The output from the laser is split into two parts by a beamsplitter. One part passes through a UV-Vis generator (optical parametric amplifier, OPA, or harmonic generation by barium borate (BBO) crystals) to change the fundamental laser to the desired pump excitation wavelength. The other part is used to generate the probe pulse. This is achieved by focusing the pulse in nonlinear crystals, where a white

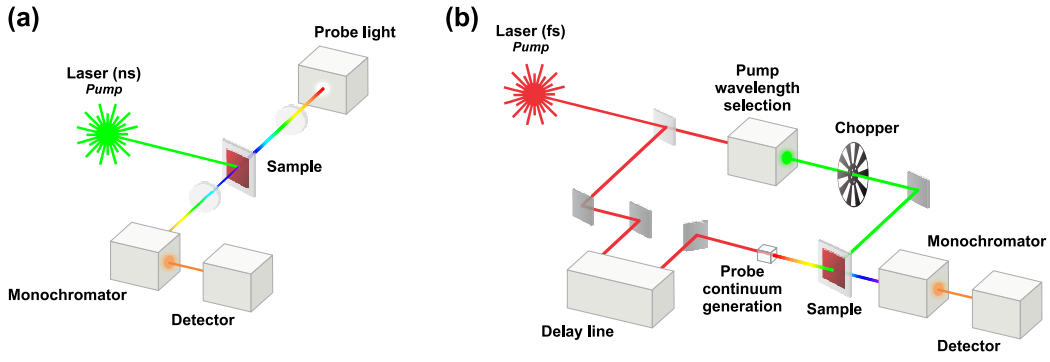

Figure 15. Schematic diagram of the components in the (a) nanosecond and (b) ultrafast pulsed laser spectroscopy setup.

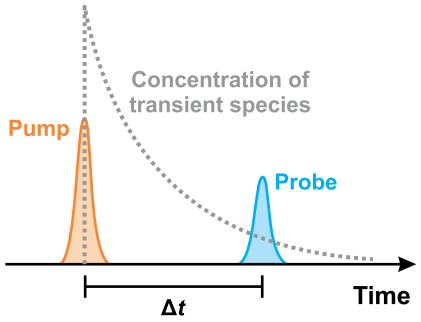

Figure 16. Schematic diagram of an ultrafast pump-probe technique, in which the changes in absorbance as a function of time resulting from different concentrations of transient species are measured at different pump-probe delay times.

(TAS) or infrared (TRIR) light continuum is generated. To vary the arrival times of the two pulses at the sample, a delay line is used in either the pump or the probe path, which consists of a retroreflector mounted on a high-precision motorized computer-controlled translation stage. The probe beam transmitted through the sample is selected by a monochromator and is detected with a suitable detector. Every other pump pulse is blocked with a synchronized chopper, and the absorbance changes are calculated with two adjacent probe pulses.[66,231-234] The changes in the absorbance $\Delta A(\lambda)$ are determined as a function of both wavelength and time by measuring the transient absorption spectra at different pump-probe delay times.

Some examples of the use of each technique for interfacial electron transfer processes are given in the following sections.

5.1.1. Transient absorption spectroscopy

Nanosecond transient absorption spectroscopy is usually employed in the investigation of the kinetics of back-electron transfer, regeneration of oxidized chromophores, catalyst activation, and recombination to oxidized species in a redox electrolyte.[18,72,138,152,235-238] Nanosecond TAS has been successfully employed to correlate the effects of the molecular engineering of dye sensitizers with the performance of DSSCs.[17,18] It was shown that the efficiency of the devices does not always follow a monotonic trend with systematic modifications on the electron donating/withdrawing ability of substituent groups in metal complexes or their steric bulk. Instead, efficiencies depend on a delicate balance between the kinetics of all the electron transfer processes that are affected in different fashions by these molecular changes. Nanosecond TAS was also appropriate to probe the light-induced redox equivalent separation and accumulation in molecular assemblies for utilization in water splitting DSPECs.[213]

In contrast to nanosecond TAS, ultrafast transient absorption spectroscopy is employed to investigate processes that occur at the subnanosecond timescale, such as electron injection from the excited chromophore into the TiO_2 acceptor states[239,240] and fast regeneration by electrolytes.[241] Ultrafast TAS allowed examining in detail the biphasic excited state electron injection process in DSSCs.[242] Additionally, this technique was used to characterize the first photoactivation step in a chromophore-catalyst assembly in water splitting DSPECs that occur in the picosecond timescale.[243]

TAS is a versatile technique that can be employed to investigate interfacial electron transfer reactions in virtually any dye-sensitized interface in which at least one of the light-induced transient species exhibits changes in its UV-Vis absorption spectra in comparison to the system before the laser pulse, and it is particularly useful when the transient species exhibit distinguished, well-defined spectral signatures. However, in some cases, the overlap of multiple contributions to the transient absorption spectra, or small ΔA values, may limit the use of the technique. Selecting a wavelength where multiple species absorb could lead to misinterpretation of the kinetics.[225]

5.1.2. Time-resolved infrared spectroscopy

Unlike most transient absorption studies in the visible region, which are hindered by the spectral overlap of absorptions by several species, such as excited state and reaction products,[244] TRIR allows us to unambiguously measure the infrared absorption changes caused by injected electrons (free carrier absorption, intraband transitions, and absorption by trap states), and the vibrational spectra of the surface-bound molecular species in their excited, oxidized and reduced states.[245-247] For molecules containing carbonyl or cyano groups, TRIR is particularly useful since the stretching of these groups gives rise to strong absorption of infrared radiation. Furthermore, these vibrations are very sensitive to changes in the electron density in the molecule and intra/intermolecular interactions, thus allowing the identification and monitoring of the temporal evolution of the excited state and different oxidation states of the surface-bound molecular species.[66,232,248]

The possibility of directly detecting electrons in nanoparticles with a sufficient time resolution makes TRIR especially useful in the investigation of the electron injection dynamics of chromophores into TiO_2 nanocrystalline thin films.[245] The subsequent back-electron transfer reaction, as well as the vibrational relaxation of excited states, chemical transformations on the surface-bound molecules, and the distribution of deep trap states on the metal oxide[66,227,249] can also be investigated by using this technique, and useful information on the mechanisms involved in energy conversion can be provided.

The recombination of electrons that were injected into TiO_2 with acceptors in the I_3^-/I^- mediator in DSSCs, when different pyridine additives were added to the electrolyte, was investigated by TRIR.[250] Pyridine additives are usually added to increase the photovoltage of the cells. It was long proposed in the literature that this enhancement was due to adsorption of the pyridine derivatives at the TiO_2 surface, blocking bare surface states that could serve as active sites for recombination with small acceptors in the mediator.[146] Surprisingly, in TRIR experiments in which the absorption decay of photogenerated electrons was monitored, it was found that these pyridine additives actually enhanced the recombination reaction in comparison with the electrolyte without any pyridine derivatives, resulting from a larger driving force for electron transfer.

TRIR was also employed to decipher the structure and lifetime of intermediates formed after photoexcitation of a chromophore in a DSPEC photocathode.[251] Although the charge transfer and recombination kinetics have previously been described for the same chromophore using TAS, the spectra contained broad features that made it difficult to resolve the excited state from the reduced dye. However, the chromophore had infrared-active nitrile groups that made it ideal for probing in the infrared. The use of TRIR spectroscopy provided a far more detailed picture of the complex series of events in the adsorbed chromophore following initial excitation. The results from that study demonstrated that fast back-electron transfer presents a limit to the performance of DSPEC photocathodes.

5.2. Small voltage and current modulation techniques

Investigations of electron transfer and transport processes in complete devices for solar energy conversion can be performed by using techniques based on the modulation of the voltage or current of the device through a small electrical or optical perturbation of its steady-state conditions. These techniques allow the simultaneous capture of snapshots of various electron transfer processes under a wide range of operating conditions. In the frequency-domain methods, the response of the device to a periodic perturbation is recorded. Alternatively, in the time-domain methods, the response of the device is monitored as a function of time following a fast perturbation.

5.2.1. Frequency-domain methods

There are a number of well-established techniques in the frequency domain that are frequently employed to elucidate *in situ* charge transfer, accumulation and transport processes in photoelectrochemical systems, most notably in DSSCs[225,252-254] and DSPECs.[209,214,217] The central frequency-domain methods are electrochemical impedance spectroscopy (EIS),[252,255-259] intensity-modulated photovoltage spectroscopy (IMVS)[107,260] and intensity-modulated photocurrent spectroscopy (IMPS).[108,261-264]

In EIS, the alternating current response of the device to a sinusoidal voltage modulation is measured as a function of the modulation frequency. On the other hand, IMVS and IMPS are based on measuring the photovoltage and photocurrent response of the device, respectively, to a sinusoidal modulation of the incident light intensity.[265] It has been shown that these techniques are interrelated and yield similar information on the dynamics of the internal components of the devices.[104,265-269]

5.2.1.1. Electrochemical impedance spectroscopy

The EIS measurements are performed by applying a small alternating, sinusoidal voltage $V(\omega,t)$ across the sample over a wide range of angular frequencies ($f = \omega/2\pi$). This periodic perturbation is superimposed on a constant potential. The alternating current output $I(\omega,t)$ is measured with respect to both the amplitude and phase shift.[257,270] This response signal has the same frequency as the applied signal, but it is phaseshifted, as shown in Figure 17. The current response is related to the time that it takes for the sample to return to equilibrium after excitation by the electrical input. The frequency window analyzed is determined by the timescales of the relaxation processes investigated.

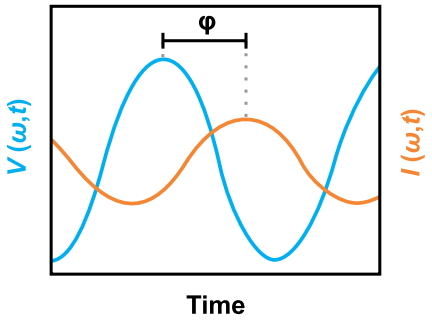

Figure 17. Representation of the sinusoidal voltage perturbation $V(\omega,t)$ and the corresponding alternating current response $I(\omega,t)$ in an EIS experiment. The phase shift φ is the time delay between the input perturbation and the output response (adapted from reference 270).

The impedance $Z(\omega)$, given by equation 27, is a complex quantity that relates the sample output to the input as a function frequency, $Z = Z' + iZ''$. Physically, the real part Z' is the resistance of the sample defined by Ohm's law. Z'' is the reactance, which describes the resistance of the sample to changes in the current flow.

$$Z(\omega) = \frac{V(t,\omega)}{I(t,\omega)} \quad (27)$$

By scanning a wide range of frequencies, typically from megahertz (microsecond) to subhertz (less than seconds), an impedance spectrum is obtained. One of the most common representations of the impedance spectrum is the Nyquist plot (–Z" *vs.* Z'). The Nyquist plot of DSSCs, for example, generally results in a shape containing three semicircles, as shown in Figure 18, each of which is assigned to a corresponding charge transfer process with a different relaxation timescale.[253,271] The first semicircle corresponds to the electron transfer reactions at the counterelectrode|electrolyte and uncovered TCO|electrolyte interfaces at high frequencies. The middle semicircle corresponds to electron diffusion in the TiO_2 film and electron recombination with oxidized species in the electrolyte at intermediate frequencies. The third semicircle, which is in the low-frequency region, corresponds to the diffusion of ions in the electrolyte.

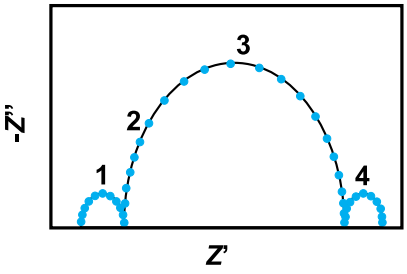

Figure 18. Representation of typical Nyquist impedance spectra of a DSSC. In the order of decreasing frequency, the regions correspond to (1) the electron transfer processes at the counterelectrode|electrolyte and uncovered TCO|electrolyte interfaces, (2) electron diffusion in the TiO_2 film, (3) electron recombination with oxidized species in the electrolyte, and (4) diffusion of redox ions in the electrolyte (adapted from references 252 and 253).

The assignment of the semicircles and the extraction of the relevant physical information come from the analysis of the impedance spectrum through fitting the data using equivalent circuit models of the device. They are composed of combinations of electrical components, such as resistors, capacitors, and nonideal elements. The most commonly used equivalent circuit is a transmission line model,[252] as shown in Figure 19. Each virtual electrical component is related to an underlying physical parameter, accounting for the various interfaces in the device. The hindrance of the charge transport in the materials and of the charge transfer across the interfaces is represented by the resistances, and the accumulation of charge is accounted for by the capacitive circuit elements.[265]

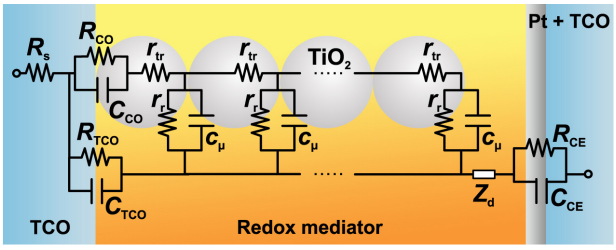

Figure 19. Complete equivalent circuit model for a DSSC (adapted from reference 272).

Following the example of a DSSC, the TCO substrate resistance is modeled by a simple resistor, R_s. R_{TCO} and C_{TCO} are the electron transfer resistance and double-layer chemical capacitance (i.e., the capability of a system to accept or release additional carriers) at the exposed TCO|electrolyte interface, respectively. R_{CO} and C_{CO} are the resistance and capacitance, respectively, at the TCO|TiO_2 interface. The mesoporous TiO_2 structure is modeled by a series of interconnected nanoparticles, each having a parallel capacitor (c_μ)|resistor (r_r) element; c_μ is the chemical capacitance of the TiO_2 film; and r_r is the resistance for the recombination between $TiO_2(e^-)$ and the oxidized species in the electrolyte. The transport resistance of electrons in/between TiO_2 nanoparticles is given by r_{tr}. The superposition of all these elements gives the mesoporous TiO_2 film's chemical capacitance C_μ, its recombination resistance R_r and its transport resistance R_{tr}. The diffusion impedance of the redox species in the electrolyte is given by Z_d and includes the diffusion of the electrolyte both in the porous TiO_2 matrix and in the bulk of the electrolyte layer between the TiO_2 film and the counterelectrode. The charge transfer resistance R_{CE} at the counter electrode is associated with the regeneration of the redox mediator, while C_{CE} is the double-layer capacitance at the same interface.[225,252,253,257,272]

Several important parameters can be determined from the impedance spectra fit parameters, which allow us to compare and correlate the EIS measurements to the photoelectrochemical performances of the devices.[179,272,273] The electron lifetime (τ_n) is the average time an electron spends in the film before recombination, as given by equation 28. The charge collection efficiency (Φ_{col}) is given by equation 29, where τ_{tr} is the electron transport time through the mesoporous film. As the electron transport in TiO_2 is diffusional, the electron transport is related to the effective diffusion coefficient of electrons D_n by equation 30, where the factor 2.77 is an approximate value that comes from the geometry of the system and d is the film thickness.[274] Finally, the electron diffusion length (L_n), which is the average length an electron moves within the TiO_2 film before recombination, is calculated from equation 31.[175,275] For good energy conversion efficiencies, the electron diffusion length should be greater than the film thickness, meaning that electrons are efficiently collected at the TCO back-contact before they recombine.

$$\tau_n = R_r \times C_\mu \quad (28)$$

$$\Phi_{col} = 1 - \frac{\tau_{tr}}{\tau_n} \quad (29)$$

$$D_n = \frac{d^2}{2.77\tau_{tr}} = \frac{d^2}{2.77 R_{tr} \times C_\mu} \quad (30)$$

$$L_n = \sqrt{D_n \times \tau_n} = d \times \sqrt{\frac{R_r}{R_{tr}}} \quad (31)$$

EIS measurements can be performed under a broad range of experimental conditions, such as background potentials varying from open to short circuit, both in the dark or under illumination, facilitating the interpretation of the spectra and the extraction of relevant physical parameters from the data, which is an unsurpassed advantage of the technique.[252,273] The equivalent circuit shown in Figure 19 may also be simplified depending on these conditions.[225]

EIS was employed to investigate the reason for the coadsorption of deoxycholic acid (DCA) to significantly improve the light-to-electrical energy conversion efficiency of DSSCs sensitized by a coumarin dye.[276] The EIS data indicated that the electron lifetimes were gradually improved with increasing content of DCA in the TiO_2 surface. The origin of the increase in electron lifetimes was tracked to the blocking effect of the DCA layer, which prevented recombination of injected electrons to the acceptors in the electrolyte.

In water splitting DSPECs, a surface-bound catalyst for water oxidation requires long-lived charge separation and the accumulation of four oxidative equivalents before back-electron transfer occurs. EIS was a suitable technique to demonstrate the dependence of back-electron transfer on the identity of the anchoring group responsible for adsorption of the catalyst onto the surface of TiO_2.[277] It was found that a pyridyl bridging ligand inhibited more efficiently back-electron transfer to a ruthenium catalyst in comparison to the broadly used phosphonate groups.

5.2.1.2. Intensity modulated photovoltage and photocurrent spectroscopies

Both IMVS and IMPS operate in manners similar to EIS.[278] However, instead of modulating the electrical input to the sample, the intensity of a light beam focused on the device is periodically modulated. This sinusoidal light modulation is superimposed on a much more intense constant background light. The photovoltage or photocurrent response is monitored. Analogous to EIS, the output response has the same frequency as the applied input, but its phase is shifted. By changing the frequency of the modulation light during the experiment, kinetic information about electron transfer and transport processes can be obtained.

IMVS is particularly useful to evaluate the electron lifetimes. In IMVS experiments, the sample is held in an open circuit, and the generated photovoltage is measured as a function of the modulated light intensity.[107,267] Usually, the imaginary part of the response signal is plotted against the real part (Nyquist plots), yielding one or more semicircles. The radius of the semicircle decreases with the increasing light intensities. The frequency f_{IMVS} at the maximum of each semicircle is related to the electron lifetime, as given by equation 32.

$$\tau_n = \frac{1}{2\pi f_{IMVS}} \quad (32)$$

In contrast, IMPS is employed to evaluate the electron transport time within the mesoporous film. The experiments are performed with the sample held under short-circuit conditions, and the response photocurrent is measured as a function of the light intensity.[267] The transport time τ_{tr} can be extracted from the maximum of the arc on the Nyquist plot of the photocurrent response, as given by equation 33.

$$\tau_{tr} = \frac{1}{2\pi f_{IMPS}} \quad (33)$$

A combination of these two techniques can be used to deconvolute the dynamics of electron transfer and transport within energy conversion devices. Furthermore, as EIS and IMVS/IMPS are interrelated, the mathematical expressions in equations 28 to 31 can be used to extract important quantities from IMVS/IMPS measurements, and both techniques yield equal estimates.

Quasi-solid DSSCs are devices in which the liquid electrolyte is replaced by a gel electrolyte, for example, based on ionic liquids such as imidazolium-based iodide salts. IMVS and IMPS were employed to explore the influence of alkyl chain length of the imidazolium cation (Im^+) on the kinetic processes of electron transport within TiO_2 and recombination of injected electrons with acceptors in the mediator.[279] It was found that longer Im^+ alkyl chains prolonged the electron lifetimes and resulted in more efficient DSSCs, but the electron transport process was slowed down. Since the cations which exist in the electrolyte such as Im^+ and Li^+ can affect the quantity and distribution of TiO_2 surface states, the conduction band edge, and the rates of electron transport and recombination, the tendencies measured by IMVS/IMPS were tracked to competitive adsorption effects of Im^+ and Li^+ on TiO_2.

Because of its slow kinetics, the water oxidation reaction is typically the limiting factor in water splitting DSPECs. In this context, IMPS and numeric simulations were employed to model the charge transport dynamics in DSPECs in conditions that mimic slow water oxidation by a catalyst at the surface of TiO_2.[217] IMPS results allowed the construction of a kinetic model describing the interplay between electron diffusion, recombination, and hole transfer to solution species that suggested that fast electron diffusion in the semiconductor, slow interfacial charge recombination, and rapid catalysis of water oxidation can improve the efficiency of DSPECs.

5.2.2. Time-domain methods

Time-domain techniques have also been used to extract key parameters related to electron transfer and transport in solar energy conversion devices, such as the electron lifetime and the diffusion coefficient of electrons in TiO_2 films.[18,194,280-282] In the time-domain methods, the measurements are made as a function of time following a single, small perturbation to the sample. These methods are advantageous over frequency-domain techniques because they allow measurements to be performed more rapidly under a wide range of operating conditions.[283] Furthermore, the information derived from the measurements is more easily extracted and interpreted without requiring complicated modeling. However, information about components other than the mesoporous photoelectrode, such as the counterelectrode or the electrolyte, cannot be easily determined from time-domain methods alone.

Transient photovoltage decay (TVD) and transient photocurrent decay (TCD) measurements are typical small-modulation methods. The measurements consist of keeping the device under operating steady-state conditions by illuminating it with a large constant bias light intensity, thus maintaining a background concentration of electrons within TiO_2. Then, a small, short pulse of light (with duration of μs-ms) is superimposed on the bias illumination, causing a perturbation in the system. Extra electrons are injected into the metal oxide, raising the TiO_2 Fermi level, the photovoltage and the photocurrent of the device. The relaxation of the system back to the starting conditions is measured by the kinetic response of the resulting photovoltage/photocurrent.[225,283] The electron transfer rate constants can be extracted by fitting the current/voltage response by single exponential functions.

TVD is primarily used to gather information about the injected electron lifetimes. The device is typically kept under open-circuit conditions so that no current flows from the cell contacts. The bias light builds a steady-state open circuit voltage in the cell, as shown in Figure 20a. Following excitation by the light pulse, as shown in Figure 20b, electron recombination of the extra injected electrons to the redox electrolyte is the only way for the system to adjust its Fermi level back to steady-state conditions, as shown in Figure 20c (the timescale of the measurement and high concentration of redox mediator in complete solar cells do not allow resolution of the back-electron transfer). The change in the concentration of electrons in TiO_2 as a function of time is measured indirectly by monitoring the cell voltage before, during, and after the pulse. The photovoltage decay lifetime is equal to the lifetime of the injected electrons.

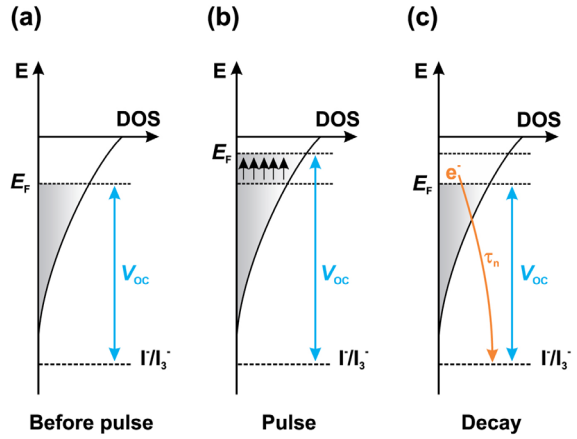

Figure 20. Schematic diagram showing the changes in the density of states of the trapped electrons as a function of energy during a transient photovoltage decay measurement.

TCD measurements are performed in a similar fashion to TVD measurements but with the cell under short-circuit conditions. Under these conditions, recombination to the acceptor species in the electrolyte is often assumed to be negligible, i.e., all injected electrons are collected.[225,284] The cell photocurrent is monitored before, during, and after the pulse. The photocurrent decay lifetime is equal to the electron transport time in TiO_2, τ_{tr}. The diffusion coefficient of electrons D_n is calculated by using equation 30.

The values related to the recombination and transport of electrons in the device depend on the steady-state condition. To obtain a complete picture of the device, the TVD and TCD experiments are repeated under many different background electron concentrations, which are achieved by changing the intensity of the incident bias light. A comparison of the electron lifetime extracted from TVD and the diffusion coefficients from the TCD measurements at matched electron concentrations allows calculation of the electron diffusion length according to equation 31.[283]

TVD and TCD techniques were combined to investigate the recombination of electrons in TiO_2 to acceptors in the mediator in a series of DSSCs in which Li^+, Na^+, Mg^{2+} or

Ca^{2+} were present in the electrolyte.[285] It was observed that the electron lifetimes τ_n at any electron concentration exhibited a clear cation-dependence that followed the trend $Na^+ < Li^+ < Mg^{2+} < Ca^{2+}$, while the diffusion coefficients D_n were independent of the electrolyte cation. Since the Lewis-acidic cations shifted the energetic position of the TiO_2 acceptor states upwards, Ca^{2+} ca. $Mg^{2+} < Li^+ < Na^+$, these results indicated that the thermodynamic driving force predominantly controls the cation-dependence of charge recombination in DSSCs, with minimal contribution from electron diffusion.[285,286]

Although these techniques are more commonly employed to study electron transfer and transport in DSSCs, TVD measurements also were reported to allow the investigation of the lifetimes of photoinjected electrons in water oxidation DSPECs.[209]

5.3. Chronoabsorptometry

Chronoabsorptometry is a spectroelectrochemical technique that has been intensively used in the investigation of lateral self-exchange reactions in dye-sensitized films.[13] Experiments can be performed by combining the use of a simple spectrophotometer and a potentiostat. The measurements consist of monitoring the optical absorption changes of the film induced by a single step change in the electrical potential applied to the sample as a function of time.

To study the hole hopping kinetics in dye-sensitized TiO_2 films, a sufficiently oxidizing potential step is applied to the sample. This applied potential continuously oxidizes the sensitizer molecules close to the TCO surface. The oxidized species are translated away from the TCO surface through lateral intermolecular self-exchange across the nanocrystalline TiO_2 surface, as shown in Figure 21a. As time progresses, the diffusion layer (or oxidation front) moves through the film until it reaches the outer edges and the film is completely oxidized.[91,183]

The spectral changes that are indicative of the electron transfer reaction are plotted as the normalized single-wavelength absorbance change, ΔA, *versus* the square root of time, $t^{1/2}$, as shown in Figure 21b. The changes in absorption are fitted to the Anson equation, as shown in equation 34, yielding the apparent diffusion coefficient D_{app}, which describes the mobility of the electrons between the anchored sensitizer molecules.[287]

$$\Delta A = \frac{2D_{app}^{1/2} t^{1/2}}{d\pi^{1/2}} \quad (34)$$

To compare the measured rates with other techniques, it is often convenient to use the measured D_{app} values

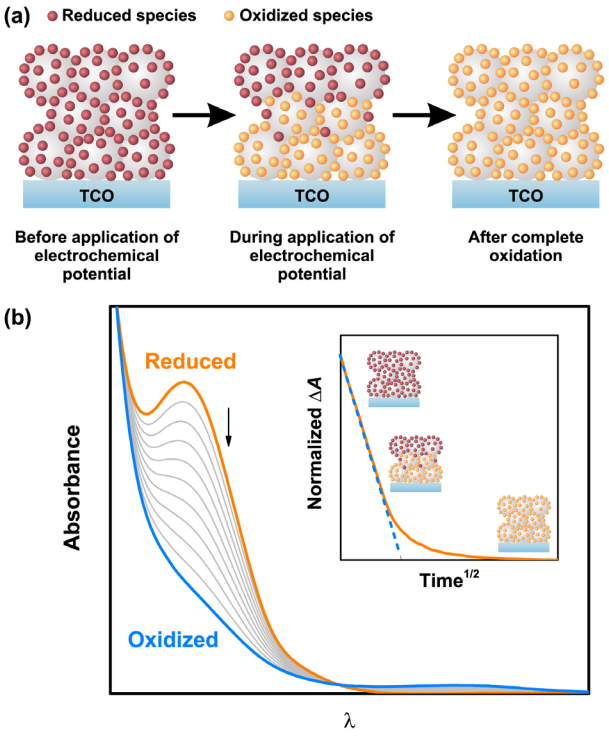

Figure 21. (a) Representation of the time evolution of the oxidation of surface-bound molecules during a chronoabsorptometry experiment (adapted from reference 91). (b) Example of absorption changes during the application of a sufficiently positive electrical potential to a dye-sensitized film. The inset shows the normalized absorbance change plotted against the square root of time, fitted by the Anson equation (blue dashed line).

to estimate the first-order effective rate constants for intermolecular hole hopping, k_{hh}, by using the Dahms-Ruff equation, which is given by equation 35.[18,288]

$$D_{app} = \frac{k_{HH}\delta^2}{n} \quad (35)$$

The conversion requires knowledge of the intermolecular distance between the molecules on the surface, δ, and the number of nearest neighbor molecules, n. These parameters are often estimated based on critical assumptions about the molecular arrangement.[91] The obtained rate constants are often analyzed within the framework of the nonadiabatic Marcus theory presented in section 2.1.

Chronoabsorptometry was employed to evidence the mechanistic understanding that dye sensitizers that undergo fast hole hopping correlate to more rapid back-electron transfer in DSSCs,[17,18] as discussed in section 4.1.4. In a series of ruthenium(II) sensitizers, the inter-dye distance on the TiO_2 surface, and consequently, their electronic coupling, was adjusted through tuning the steric bulk of substituent groups in the ligands.[18] The sensitizers with the bulkier substituents exhibited faster hole hopping kinetics and followed the same trends measured for back-electron

transfer by TAS. These results demonstrated that the undesirable back-electron transfer pathway can be inhibited through control of lateral hole hopping by the molecular engineering of the dye sensitizer.

The choice of the solvent used in the sensitization process had a significant effect on the performance of water splitting DSPECs. To track the causes, the lateral translation of oxidized chromophores in DSPECs was investigated by chronoabsorptometry.[214] It was observed that when the sensitizer was adsorbed onto the TiO_2 surface from aqueous acid instead of water or organic solvents, the intermolecular hole hopping between photo-oxidized sensitizer molecules was significantly faster, and the D_{app} values were one order of magnitude higher. Based on previous studies, the authors suggested that small, interfacial protons may help to lower the reorganization energy for hole hopping, or that protonation may lead to a difference in the binding mode of the surface-bound sensitizer that can change the electronic coupling.[289]

6. Final Remarks

With a wide range of techniques available to elucidate the kinetics of interfacial electron transfer processes and electron transport within metal oxide films, on various timescales and with the possibility of investigating different experimental conditions (from dye-sensitized films immersed in neat solvents to complete devices under operating conditions), it is possible to obtain deep insights into the mechanisms that promote or inhibit solar energy conversion. The effects of changes on the molecular structure of the dye sensitizer and/or catalyst, on the morphology of the semiconductor oxide film, or on the composition of the electrolytes on each individual electron transfer reaction can be understood, as well as how they affect the whole picture of the device.

The kinetic investigation of the competing interfacial electron transfer reactions provides powerful information towards improving the efficiency of the devices. The analysis of the data in the framework of the Marcus and Marcus-Gerischer theories provides even more powerful tools to guide molecular engineering and the rational design of new devices. Although significant progress has been achieved since the publication of the first TiO_2 molecular device, numerous challenges remain with respect to bridging the gap between the present use of solar energy and its potential using the molecular devices presented herein, or others which are beyond the scope of this review. Some of the obstacles that must be overcome include avoiding unproductive electron transfer pathways while favoring forward electron transfer processes, accumulating multiple redox equivalents at the catalysts, and increasing the visible light harvesting ability of the chromophores.

The answer may not be clear, but a profound understanding of the fundamental aspects of interfacial electron transfer kinetics in dye-sensitized TiO_2 devices for energy conversion is the leading strategy towards a more sustainable future.

Acknowledgments

The authors are grateful to Fundação de Amparo à Pesquisa do Estado de São Paulo (FAPESP) for financial support (grants 2019/23277-4, 2016/24020-9, 2018/08038-0, 2018/24622-4, and 2018/24609-8).

Author Contributions

Andressa V. Müller was responsible for conceptualization, funding acquisition, investigation, visualization, writing original draft, and writing-review and editing; Wendel W. Magalhães and Mariana N. Pastorelli for funding acquisition, investigation, visualization, and writing original draft; André S. Polo was responsible for conceptualization, funding acquisition, investigation, project administration, supervision, visualization, writing original draft, and writing-review and editing.

Andressa V. Müller *obtained her bachelor's degree in Science and Technology (2014) and in Chemistry (2015) and her master's degree in Nanoscience and Advanced Materials (2017) from Universidade Federal do ABC (Santo André, Brazil). More recently, she received her PhD degree in Nanoscience and Advanced Materials (2021) under the supervision of Prof André S. Polo at the Laboratory of Photochemistry, Photophysics and Energy Conversion, Universidade Federal do ABC. Her current research interests focus on the molecular engineering of coordination compounds for solar-to-electrical and solar-to-chemical energy conversion and on the electron transfer processes in these systems.*

Wendel M. Wierzba *obtained his bachelor's degree in Science and Technology (2020) and in Chemistry (2021) from Universidade Federal do ABC (Santo André, Brazil). He is currently pursuing his master's degree in Nanoscience*

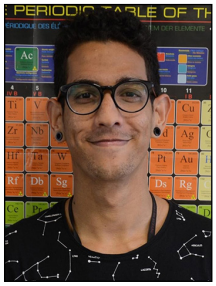

and Advanced Materials under the supervision of Prof André S. Polo at the Laboratory of Photochemistry, Photophysics and Energy Conversion, Universidade Federal do ABC. His research interest involves the investigation of systems based on Ru(II) and Re(I) coordination compounds for the conversion of solar energy. His current research topics include the investigation of electron transfer kinetics in donor-bridge-acceptor molecular systems applied to CO_2 photoreduction.

Mariana N. Pastorelli *is pursuing her bachelor's degrees in Science and Technology and in Chemistry from Federal University of ABC. Her research focus is on the electron transfer process in photochemical systems based on coordination compounds.*

André S. Polo *received his PhD in Chemistry from the Chemistry Institute at the University of São Paulo, Brazil. In 2009, he joined the Universidade Federal do ABC, where he is now an Associate Professor. His current research interests focus on comprehending the fundamental chemical processes of the coordination compounds and inorganic materials involved in solar energy conversion.*

References

1. International Energy Agency; *World Energy Outlook 2019*; https://www.iea.org/reports/world-energy-outlook-2019, accessed in May 2021.
2. United Nations Development Program; *World Energy Assessment Report: Energy and the Challenge of Sustainability*; https://sustainabledevelopment.un.org/content/documents/2423World_Energy_Assessment_2000.pdf, accessed on May 27, 2020.
3. Lewis, N. S.; Nocera, D. G.; *Proc. Natl. Acad. Sci. U. S. A.* **2006**, *103*, 15729.
4. Barber, J.; *Chem. Soc. Rev.* **2009**, *38*, 185.
5. REN21; *Renewables 2020 Global Status Report*; https://www.ren21.net/wp-content/uploads/2019/05/gsr_2020_full_report_en.pdf, accessed in May 2021.
6. Cook, T. R.; Dogutan, D. K.; Reece, S. Y.; Surendranath, Y.; Teets, T. S.; Nocera, D. G.; *Chem. Rev.* **2010**, *110*, 6474.
7. Frin, K. P. M.; da Rocha, D. C.; Mamud, J. F.; Polo, A. S.; *Photochem. Photobiol. Sci.* **2018**, *17*, 1443.
8. Mamud, J. F.; Biazolla, G.; Marques, C. S.; Cerchiaro, G.; de Queiroz, T. B.; Keppler, A. F.; Polo, A. S.; *Inorg. Chim. Acta* **2021**, *514*, 120009.
9. Passalacqua, R.; Perathoner, S.; Centi, G.; *J. Energy Chem.* **2017**, *26*, 219.
10. Pellegrin, Y.; Odobel, F.; *Coord. Chem. Rev.* **2011**, *255*, 2578.
11. Colasson, B.; Credi, A.; Ragazzon, G.; *Coord. Chem. Rev.* **2016**, *325*, 125.
12. Coggins, M. K.; Meyer, T. J. In *Photoelectrochemical Solar Fuel Production: From Basic Principles to Advanced Devices*; Giménez, S.; Bisquert, J., eds.; Springer International Publishing: Cham, Switzerland, 2016.
13. Li, X.; Nazeeruddin, M. K.; Thelakkat, M.; Barnes, P. R. F.; Vilar, R.; Durrant, J. R.; *Phys. Chem. Chem. Phys.* **2011**, *13*, 1575.
14. Paolella, A.; Faure, C.; Bertoni, G.; Marras, S.; Guerfi, A.; Darwiche, A.; Hovington, P.; Commarieu, B.; Wang, Z.; Prato, M.; Colombo, M.; Monaco, S.; Zhu, W.; Feng, Z.; Vijh, A.; George, C.; Demopoulos, G. P.; Armand, M.; Zaghib, K.; *Nat. Commun.* **2017**, *8*, 14643.
15. Zambiazi, P. J.; de Moraes, A. T. N.; Kogachi, R. R.; Aparecido, G. O.; Formiga, A. L. B.; Bonacin, J. A.; *J. Braz. Chem. Soc.* **2020**, *31*, 2307.
16. Müller, A. V.; Ramos, L. D.; Frin, K. P. M.; de Oliveira, K. T.; Polo, A. S.; *RSC Adv.* **2016**, *6*, 46487.
17. Sampaio, R. N.; Müller, A. V.; Polo, A. S.; Meyer, G. J.; *ACS Appl. Mater. Interfaces* **2017**, *9*, 33446.
18. Müller, A. V.; de Oliveira, K. T.; Meyer, G. J.; Polo, A. S.; *ACS Appl. Mater. Interfaces* **2019**, *11*, 43223.
19. Hagfeldt, A.; Boschloo, G.; Sun, L.; Kloo, L.; Pettersson, H.; *Chem. Rev.* **2010**, *110*, 6595.
20. O'Regan, B.; Grätzel, M.; *Nature* **1991**, *353*, 737.
21. Sun, Y.; Onicha, A. C.; Myahkostupov, M.; Castellano, F. N.; *ACS Appl. Mater. Interfaces* **2010**, *2*, 2039.
22. de Souza, J. S.; de Andrade, L. O. M.; Müller, A. V.; Polo, A. S. In *Nanoenergy: Nanotechnology Applied for Energy Production*, 2nd ed.; Souza, F. L.; Leite, E. R., eds.; Springer International Publishing: Cham, Switzerland, 2018.
23. Gratzel, M.; *Nature* **2001**, *414*, 338.
24. Grätzel, M.; *J. Photochem. Photobiol., C* **2003**, *4*, 145.
25. Grätzel, M.; *Inorg. Chem.* **2005**, *44*, 6841.
26. Grätzel, M.; *Philos. Trans. R. Soc., A* **2007**, *365*, 993.
27. Nazeeruddin, M. K.; Baranoff, E.; Grätzel, M.; *Sol. Energy* **2011**, *85*, 1172.
28. Pashaei, B.; Shahroosvand, H.; Graetzel, M.; Nazeeruddin, M. K.; *Chem. Rev.* **2016**, *116*, 9485.
29. Nunes, B. N.; Faustino, L. A.; Müller, A. V.; Polo, A. S.; Patrocinio, A. O. T. In *Nanomaterials for Solar Cell*

Applications, 1st ed.; Thomas, S.; Sakho, E. H. M.; Kalarikkal, N.; Oluwafemi, S. O.; Wu, J., eds.; Elsevier: Amsterdam, Netherlands, 2019, ch. 8.
30. Naik, P.; Su, R.; Elmorsy, M. R.; El-Shafei, A.; Adhikari, A. V.; *J. Energy Chem.* **2018**, *27*, 351.
31. Lee, M. W.; Kim, J. Y.; Lee, H. G.; Cha, H. G.; Lee, D. H.; Ko, M. J.; *J. Energy Chem.* **2021**, *54*, 208.
32. Badran, I.; Tighadouini, S.; Radi, S.; Zarrouk, A.; Warad, I.; *J. Mol. Struct.* **2021**, *1229*, 129799.
33. Hasan, M. M.; Islam, M. D.; Rashid, T. U.; *Energy Fuels* **2020**, *34*, 15634.
34. Chandra Sil, M.; Chen, L. S.; Lai, C. W.; Lee, Y. H.; Chang, C. C.; Chen, C. M.; *J. Power Sources* **2020**, *479*, 229095.
35. Orhan, E.; Gökçen, M.; Taran, S.; *Bull. Mater. Sci.* **2021**, *44*, 60.
36. Han, R.; Kim, T. Y.; Hamann, T. W.; Osterloh, F. E.; *J. Phys. Chem. C* **2020**, *124*, 26174.
37. Muchuweni, E.; Martincigh, B. S.; Nyamori, V. O.; *RSC Adv.* **2020**, *10*, 44453.
38. Meyer, T. J.; *Acc. Chem. Res.* **1989**, *22*, 163.
39. Alstrum-Acevedo, J. H.; Brennaman, M. K.; Meyer, T. J.; *Inorg. Chem.* **2005**, *44*, 6802.
40. Concepcion, J. J.; Jurss, J. W.; Brennaman, M. K.; Hoertz, P. G.; Patrocinio, A. O. T.; Iha, N. Y. M.; Templeton, J. L.; Meyer, T. J.; *Acc. Chem. Res.* **2009**, *42*, 1954.
41. Brennaman, M. K.; Dillon, R. J.; Alibabaei, L.; Gish, M. K.; Dares, C. J.; Ashford, D. L.; House, R. L.; Meyer, G. J.; Papanikolas, J. M.; Meyer, T. J.; *J. Am. Chem. Soc.* **2016**, *138*, 13085.
42. Meyer, T. J.; Sheridan, M. V.; Sherman, B. D.; *Chem. Soc. Rev.* **2017**, *46*, 6148.
43. Dogutan, D. K.; Nocera, D. G.; *Acc. Chem. Res.* **2019**, *52*, 3143.
44. Nocera, D. G.; *Acc. Chem. Res.* **2012**, *45*, 767.
45. Dempsey, J. L.; Esswein, A. J.; Manke, D. R.; Rosenthal, J.; Soper, J. D.; Nocera, D. G.; *Inorg. Chem.* **2005**, *44*, 6879.
46. Li, L.; Duan, L.; Xu, Y.; Gorlov, M.; Hagfeldt, A.; Sun, L.; *Chem. Commun.* **2010**, *46*, 7307.
47. Ding, X.; Gao, Y.; Zhang, L.; Yu, Z.; Liu, J.; Sun, L.; *ACS Catal.* **2014**, *4*, 2347.
48. Alibabaei, L.; Sherman, B. D.; Norris, M. R.; Brennaman, M. K.; Meyer, T. J.; *Proc. Natl. Acad. Sci. U. S. A.* **2015**, *112*, 5899.
49. Alibabaei, L.; Dillon, R. J.; Reilly, C. E.; Brennaman, M. K.; Wee, K. R.; Marquard, S. L.; Papanikolas, J. M.; Meyer, T. J.; *ACS Appl. Mater. Interfaces* **2017**, *9*, 39018.
50. Alibabaei, L.; Brennaman, M. K.; Norris, M. R.; Kalanyan, B.; Song, W.; Losego, M. D.; Concepcion, J. J.; Binstead, R. A.; Parsons, G. N.; Meyer, T. J.; *Proc. Natl. Acad. Sci. U. S. A.* **2013**, *110*, 20008.
51. Shan, B.; Das, A. K.; Marquard, S.; Farnum, B. H.; Wang, D.; Bullock, R. M.; Meyer, T. J.; *Energy Environ. Sci.* **2016**, *9*, 3693.
52. Sheridan, M. V.; Sherman, B. D.; Xie, Y.; Wang, Y.; *Sol. RRL* **2021**, 2000565.
53. Stolarczyk, J. K.; Bhattacharyya, S.; Polavarapu, L.; Feldmann, J.; *ACS Catal.* **2018**, *8*, 3602.
54. Takeda, H.; Ishitani, O.; *Coord. Chem. Rev.* **2010**, *254*, 346.
55. Yamazaki, Y.; Takeda, H.; Ishitani, O.; *J. Photochem. Photobiol., C* **2015**, *25*, 106.
56. Kuramochi, Y.; Ishitani, O.; Ishida, H.; *Coord. Chem. Rev.* **2018**, *373*, 333.
57. Morris, A. J.; Meyer, G. J.; Fujita, E.; *Acc. Chem. Res.* **2009**, *42*, 1983.
58. Agarwal, J.; Fujita, E.; Schaefer, H. F.; Muckerman, J. T.; *J. Am. Chem. Soc.* **2012**, *134*, 5180.
59. Fujita, E.; Muckerman, J. T.; Himeda, Y.; *Biochim. Biophys. Acta, Bioenerg.* **2013**, *1827*, 1031.
60. Schneider, J.; Jia, H. F.; Muckerman, J. T.; Fujita, E.; *Chem. Soc. Rev.* **2012**, *41*, 2036.
61. Manbeck, G. F.; Fujita, E.; *J. Porphyrins Phthalocyanines* **2015**, *19*, 45.
62. Yui, T.; Tamaki, Y.; Sekizawa, K.; Ishitani, O. In *Photocatalysis*, vol. 303; Bignozzi, C. A., ed.; Springer-Verlag Berlin: Berlin, Germany, 2011.
63. Takeda, H.; Cometto, C.; Ishitani, O.; Robert, M.; *ACS Catal.* **2017**, *7*, 70.
64. Faustino, L. A.; Souza, B. L.; Nunes, B. N.; Duong, A. T.; Sieland, F.; Bahnemann, D. W.; Patrocinio, A. O. T.; *ACS Sustainable Chem. Eng.* **2018**, *6*, 6073.
65. Windle, C. D.; Pastor, E.; Reynal, A.; Whitwood, A. C.; Vaynzof, Y.; Durrant, J. R.; Perutz, R. N.; Reisner, E.; *Chem. - Eur. J.* **2015**, *21*, 3746.
66. Abdellah, M.; El-Zohry, A. M.; Antila, L. J.; Windle, C. D.; Reisner, E.; Hammarström, L.; *J. Am. Chem. Soc.* **2017**, *139*, 1226.
67. Kamata, R.; Kumagai, H.; Yamazaki, Y.; Sahara, G.; Ishitani, O.; *ACS Appl. Mater. Interfaces* **2019**, *11*, 5632.
68. Souza, D. H. P.; Guimarães, R. R.; Correra, T. C.; Zamarion, V. M.; *New J. Chem.* **2018**, *42*, 18259.
69. Hagfeldt, A.; Cappel, U. B.; Boschloo, G.; Sun, L.; Kloo, L.; Pettersson, H.; Gibson, E. A. In *Practical Handbook of Photovoltaics*, 2nd ed.; McEvoy, A.; Markvart, T.; Castañer, L., eds.; Academic Press: Boston, United States, 2012, ch. IE-1.
70. Hu, K.; Sampaio, R. N.; Schneider, J.; Troian-Gautier, L.; Meyer, G. J.; *J. Am. Chem. Soc.* **2020**, *142*, 16099.
71. Veiga, E. T.; Müller, A. V.; Ramos, L. D.; Frin, K. P. M.; Polo, A. S.; *Eur. J. Inorg. Chem.* **2018**, *2018*, 2680.
72. Wang, X.; Li, C.; *J. Photochem. Photobiol., C* **2017**, *33*, 165.
73. Martín, C.; Ziółek, M.; Douhal, A.; *J. Photochem. Photobiol., C* **2016**, *26*, 1.
74. Zhang, L.; Mohamed, H. H.; Dillert, R.; Bahnemann, D.; *J. Photochem. Photobiol., C* **2012**, *13*, 263.
75. Marcus, R. A.; *J. Chem. Phys.* **1956**, *24*, 966.
76. Marcus, R. A.; *J. Chem. Phys.* **1957**, *26*, 867.

77. Marcus, R. A.; *J. Chem. Phys.* **1957**, *26*, 872.
78. Marcus, R. A.; *Discuss. Faraday Soc.* **1960**, *29*, 21.
79. Marcus, R. A.; *J. Phys. Chem.* **1963**, *67*, 853.
80. Marcus, R. A.; *J. Chem. Phys.* **1965**, *43*, 679.
81. Marcus, R. A.; Sutin, N.; *Biochim. Biophys. Acta, Bioenerg.* **1985**, *811*, 265.
82. Marcus, R. A.; *Angew. Chem., Int. Ed.* **1993**, *32*, 1111.
83. Barbara, P. F.; Meyer, T. J.; Ratner, M. A.; *J. Phys. Chem.* **1996**, *100*, 13148.
84. Gerischer, H.; *Z. Phys. Chem.* **1960**, *26*, 223.
85. Gerischer, H.; *Surf. Sci.* **1969**, *18*, 97.
86. Piechota, E. J.; Meyer, G. J.; *J. Chem. Educ.* **2019**, *96*, 2450.
87. Memming, R; *Semiconductor Electrochemistry*, 2nd ed.; Wiley: Weinheim, Germany, 2015.
88. Marcus, R. A.; *Pure Appl. Chem.* **1997**, *69*, 13.
89. Schmickler, W.; *J. Electroanal. Chem. Interfacial Electrochem.* **1986**, *204*, 31.
90. Robin, M. B.; Day, P. In *Advances in Inorganic Chemistry and Radiochemistry*, vol. 10; Emeléus, H. J.; Sharpe, A. G., eds.; Academic Press: New York, United States, 1968.
91. Motley, T. C.; Brady, M. D.; Meyer, G. J.; *J. Phys. Chem. C* **2018**, *122*, 19385.
92. Kuss-Petermann, M.; Wenger, O. S.; *Phys. Chem. Chem. Phys.* **2016**, *18*, 18657.
93. Closs, G. L.; Miller, J. R.; *Science* **1988**, *240*, 440.
94. Gerischer, H.; *J. Phys. Chem.* **1991**, *95*, 1356.
95. Greiner, M. T.; Lu, Z.-H.; *NPG Asia Mater.* **2013**, *5*, e55.
96. Asahi, R.; Taga, Y.; Mannstadt, W.; Freeman, A. J.; *Phys. Rev. B* **2000**, *61*, 7459.
97. Pankove, J. I.; *Optical Processes in Semiconductors*; Dover Publications: New York, United States, 1975.
98. Wang, Y.; Wu, D.; Fu, L. M.; Ai, X. C.; Xu, D.; Zhang, J. P.; *ChemPhysChem* **2015**, *16*, 2253.
99. Westermark, K.; Henningsson, A.; Rensmo, H.; Södergren, S.; Siegbahn, H.; Hagfeldt, A.; *Chem. Phys.* **2002**, *285*, 157.
100. Howe, R. F.; Gratzel, M.; *J. Phys. Chem.* **1987**, *91*, 3906.
101. Thompson, T. L.; Yates, J. T.; *Chem. Rev.* **2006**, *106*, 4428.
102. O'Donnell, R. M.; Sampaio, R. N.; Barr, T. J.; Meyer, G. J.; *J. Phys. Chem. C* **2014**, *118*, 16976.
103. Kelly, C. A.; Farzad, F.; Thompson, D. W.; Stipkala, J. M.; Meyer, G. J.; *Langmuir* **1999**, *15*, 7047.
104. Bisquert, J.; Vikhrenko, V. S.; *J. Phys. Chem. B* **2004**, *108*, 2313.
105. Schlichthörl, G.; Park, N. G.; Frank, A. J.; *J. Phys. Chem. B* **1999**, *103*, 782.
106. Adachi, M.; Murata, Y.; Takao, J.; Jiu, J.; Sakamoto, M.; Wang, F.; *J. Am. Chem. Soc.* **2004**, *126*, 14943.
107. Schlichthörl, G.; Huang, S. Y.; Sprague, J.; Frank, A. J.; *J. Phys. Chem. B* **1997**, *101*, 8141.
108. Franco, G.; Gehring, J.; Peter, L. M.; Ponomarev, E. A.; Uhlendorf, I.; *J. Phys. Chem. B* **1999**, *103*, 692.
109. van de Lagemaat, J.; Frank, A. J.; *J. Phys. Chem. B* **2000**, *104*, 4292.
110. Bisquert, J.; Fabregat-Santiago, F.; Mora-Seró, I.; Garcia-Belmonte, G.; Barea, E. M.; Palomares, E.; *Inorg. Chim. Acta* **2008**, *361*, 684.
111. Gerischer, H.; *Photochem. Photobiol.* **1972**, *16*, 243.
112. Gerischer, H.; Willig, F. In *Physical and Chemical Applications of Dyestuffs*; Schäfer, F. P.; Gerischer, H.; Willig, F.; Meier, H.; Jahnke, H.; Schönborn, M.; Zimmermann, G., eds.; Springer Berlin Heidelberg: Heidelberg, Germany, 1976.
113. Watson, D. F.; Meyer, G. J.; *Annu. Rev. Phys. Chem.* **2005**, *56*, 119.
114. Ardo, S.; Meyer, G. J.; *Chem. Soc. Rev.* **2009**, *38*, 115.
115. Aghazada, S.; Nazeeruddin, M. K.; *Inorganics* **2018**, *6*, 34.
116. Schneider, J.; Bangle, R. E.; Swords, W. B.; Troian-Gautier, L.; Meyer, G. J.; *J. Am. Chem. Soc.* **2019**, *141*, 9758.
117. Farnum, B. H.; Morseth, Z. A.; Brennaman, M. K.; Papanikolas, J. M.; Meyer, T. J.; *J. Phys. Chem. B* **2015**, *119*, 7698.
118. Bangle, R. E.; Schneider, J.; Piechota, E. J.; Troian-Gautier, L.; Meyer, G. J.; *J. Am. Chem. Soc.* **2020**, *142*, 674.
119. Sakata, T.; Hashimoto, K.; Hiramoto, M.; *J. Phys. Chem.* **1990**, *94*, 3040.
120. Kitao, O.; *J. Phys. Chem. C* **2007**, *111*, 15889.
121. Gawęda, S.; Podborska, A.; Macyk, W.; Szaciłowski, K.; *Nanoscale* **2009**, *1*, 299.
122. Litter, M. I.; San Román, E.; Grela, t. l. M. A.; Meichtry, J. M.; Rodríguez, H. B. In *Visible Light-Active Photocatalysis: Nanostructured Catalyst Design, Mechanisms, and Applications*; Ghosh, S., ed.; Wiley-VCH: Weinheim, Germany, 2018, ch. 10.
123. Buchalska, M.; Łabuz, P.; Bujak, Ł.; Szewczyk, G.; Sarna, T.; Maćkowski, S.; Macyk, W.; *Dalton Trans.* **2013**, *42*, 9468.
124. Durrant, J. R.; Haque, S. A.; Palomares, E.; *Coord. Chem. Rev.* **2004**, *248*, 1247.
125. Creutz, C.; Brunschwig, B. S.; Sutin, N.; *J. Phys. Chem. B* **2005**, *109*, 10251.
126. Creutz, C.; Brunschwig, B. S.; Sutin, N.; *Chem. Phys.* **2006**, *324*, 244.
127. Creutz, C.; Brunschwig, B. S.; Sutin, N.; *J. Phys. Chem. B* **2006**, *110*, 25181.
128. Barzykin, A. V.; Tachiya, M.; *J. Phys. Chem. B* **2002**, *106*, 4356.
129. Hasselmann, G. M.; Meyer, G. J.; *J. Phys. Chem. B* **1999**, *103*, 7671.
130. Nelson, J.; *Phys. Rev. B* **1999**, *59*, 15374.
131. Nelson, J.; Haque, S. A.; Klug, D. R.; Durrant, J. R.; *Phys. Rev. B* **2001**, *63*, 205321.
132. Villanueva-Cab, J.; Wang, H.; Oskam, G.; Peter, L. M.; *J. Phys. Chem. Lett.* **2010**, *1*, 748.
133. Barnes, P. R. F.; O'Regan, B. C.; *J. Phys. Chem. C* **2010**, *114*, 19134.
134. Liu, X.; Zhang, Q.; Li, J.; Valanoor, N.; Tang, X.; Cao, G.; *Sci. Rep.* **2018**, *8*, 17389.

135. Hagfeldt, A.; Grätzel, M.; *Chem. Rev.* **1995**, *95*, 49.
136. Albery, W. J.; *J. Electrochem. Soc.* **1984**, *131*, 315.
137. Zhang, Z.; Yates, J. T.; *Chem. Rev.* **2012**, *112*, 5520.
138. Katoh, R.; Furube, A.; Barzykin, A. V.; Arakawa, H.; Tachiya, M.; *Coord. Chem. Rev.* **2004**, *248*, 1195.
139. Bisquert, J.; *J. Phys. Chem. C* **2007**, *111*, 17163.
140. Adhikari, P.; Kobbekaduwa, K.; Shi, Y.; Zhang, J.; Abass, N. A.; He, J.; Rao, A.; Gao, J.; *Appl. Phys. Lett.* **2018**, *113*, 183509.
141. Saygili, Y.; Stojanovic, M.; Flores-Díaz, N.; Zakeeruddin, S. M.; Vlachopoulos, N.; Grätzel, M.; Hagfeldt, A.; *Inorganics* **2019**, *7*, 30.
142. Bignozzi, C. A.; Argazzi, R.; Boaretto, R.; Busatto, E.; Carli, S.; Ronconi, F.; Caramori, S.; *Coord. Chem. Rev.* **2013**, *257*, 1472.
143. Reynal, A.; Palomares, E.; *Eur. J. Inorg. Chem.* **2011**, 4509.
144. Carvalho, F.; Liandra-Salvador, E.; Bettanin, F.; Souza, J. S.; Homem-de-Mello, P.; Polo, A. S.; *Inorg. Chim. Acta* **2014**, *414*, 145.
145. Müller, A. V.; Mendonça, P. S.; Parant, S.; Duchanois, T.; Gros, P. C.; Beley, M.; Polo, A. S.; *J. Braz. Chem. Soc.* **2015**, *26*, 2224.
146. Nazeeruddin, M. K.; Kay, A.; Rodicio, I.; Humphry-Baker, R.; Muller, E.; Liska, P.; Vlachopoulos, N.; Grätzel, M.; *J. Am. Chem. Soc.* **1993**, *115*, 6382.
147. Müller, A. V.; Polo, A. S.; *Inorg. Chem.* **2018**, *57*, 13829.
148. Hu, Y.; Robertson, N.; *Front. Optoelectron.* **2016**, *9*, 38.
149. Wang, Z. S.; Koumura, N.; Cui, Y.; Takahashi, M.; Sekiguchi, H.; Mori, A.; Kubo, T.; Furube, A.; Hara, K.; *Chem. Mater.* **2008**, *20*, 3993.
150. Sathiyan, G.; Sivakumar, E. K. T.; Ganesamoorthy, R.; Thangamuthu, R.; Sakthivel, P.; *Tetrahedron Lett.* **2016**, *57*, 243.
151. Hara, K.; Sato, T.; Katoh, R.; Furube, A.; Yoshihara, T.; Murai, M.; Kurashige, M.; Ito, S.; Shinpo, A.; Suga, S.; Arakawa, H.; *Adv. Funct. Mater.* **2005**, *15*, 246.
152. Hara, K.; Wang, Z. S.; Sato, T.; Furube, A.; Katoh, R.; Sugihara, H.; Dan-Oh, Y.; Kasada, C.; Shinpo, A.; Suga, S.; *J. Phys. Chem. B* **2005**, *109*, 15476.
153. Mishra, A.; Fischer, M. K.; Bäuerle, P.; *Angew. Chem., Int. Ed. Engl.* **2009**, *48*, 2474.
154. Shalini, S.; Prabhu, R. B.; Prasanna, S.; Mallick, T. K.; Senthilarasu, S.; *Renewable Sustainable Energy Rev.* **2015**, *51*, 1306.
155. Ludin, N. A.; Mahmoud, A.; Mohamad, A. B.; Kadhum, A. A. H.; Sopian, K.; Karim, N. S. A.; *Renewable Sustainable Energy Rev.* **2014**, *31*, 386.
156. Polo, A. S.; Murakami Iha, N. Y.; *Sol. Energy Mater. Sol. Cells* **2006**, *90*, 1936.
157. Jalali, T.; Arkian, P.; Golshan, M.; Jalali, M.; Osfouri, S.; *Opt. Mater.* **2020**, *110*, 110441.
158. Theerthagiri, J.; Senthil, A. R.; Madhavan, J.; Maiyalagan, T.; *ChemElectroChem* **2015**, *2*, 928.
159. Boschloo, G.; Hagfeldt, A.; *Acc. Chem. Res.* **2009**, *42*, 1819.
160. Katoh, R.; Furube, A.; *J. Photochem. Photobiol., C* **2014**, *20*, 1.
161. Koops, S. E.; O'Regan, B. C.; Barnes, P. R. F.; Durrant, J. R.; *J. Am. Chem. Soc.* **2009**, *131*, 4808.
162. Moser, J. E.; Wolf, M.; Lenzmann, F.; Grätzel, M.; *Z. Phys. Chem.* **1999**, *212*, 85.
163. Asbury, J. B.; Anderson, N. A.; Hao, E.; Ai, X.; Lian, T.; *J. Phys. Chem. B* **2003**, *107*, 7376.
164. Ladomenou, K.; Kitsopoulos, T. N.; Sharma, G. D.; Coutsolelos, A. G.; *RSC Adv.* **2014**, *4*, 21379.
165. Kilså, K.; Mayo, E. I.; Brunschwig, B. S.; Gray, H. B.; Lewis, N. S.; Winkler, J. R.; *J. Phys. Chem. B* **2004**, *108*, 15640.
166. Zhang, L.; Cole, J. M.; *ACS Appl. Mater. Interfaces* **2015**, *7*, 3427.
167. O'Rourke, C.; Bowler, D. R.; *J. Phys.: Condens. Matter* **2014**, *26*, 195302.
168. Sen, A.; Kupfer, S.; Gräfe, S.; Groβ, A.; *J. Phys. B: At., Mol. Opt. Phys.* **2020**, *53*, 234001.
169. Clifford, J. N.; Palomares, E.; Nazeeruddin, M. K.; Grätzel, M.; Durrant, J. R.; *J. Phys. Chem. C* **2007**, *111*, 6561.
170. Robson, K. C. D.; Hu, K.; Meyer, G. J.; Berlinguette, C. P.; *J. Am. Chem. Soc.* **2013**, *135*, 1961.
171. Planells, M.; Pelleja, L.; Clifford, J. N.; Pastore, M.; de Angelis, F.; Lopez, N.; Marder, S. R.; Palomares, E.; *Energy Environ. Sci.* **2011**, *4*, 1820.
172. Feldt, S. M.; Lohse, P. W.; Kessler, F.; Nazeeruddin, M. K.; Grätzel, M.; Boschloo, G.; Hagfeldt, A.; *Phys. Chem. Chem. Phys.* **2013**, *15*, 7087.
173. Peter, L. M.; *J. Phys. Chem. C* **2007**, *111*, 6601.
174. Nelson, J.; Chandler, R. E.; *Coord. Chem. Rev.* **2004**, *248*, 1181.
175. Bisquert, J.; Fabregat-Santiago, F.; Mora-Seró, I.; Garcia-Belmonte, G.; Giménez, S.; *J. Phys. Chem. C* **2009**, *113*, 17278.
176. Yella, A.; Lee, H.-W.; Tsao, H. N.; Yi, C.; Chandiran, A. K.; Nazeeruddin, M. K.; Diau, E. W.-G.; Yeh, C.-Y.; Zakeeruddin, S. M.; Grätzel, M.; *Science* **2011**, *334*, 629.
177. Kim, D. H.; Woodroof, M.; Lee, K.; Parsons, G. N.; *ChemSusChem* **2013**, *6*, 1014.
178. Xi-Zhe, L.; Zhen, H.; Ke-Xin, L.; Hong, L.; Dong-Mei, L.; Li-Quan, C.; Qing-Bo, M.; *Chin. Phys. Lett.* **2006**, *23*, 2606.
179. Góes, M. S.; Joanni, E.; Muniz, E. C.; Savu, R.; Habeck, T. R.; Bueno, P. R.; Fabregat-Santiago, F.; *J. Phys. Chem. C* **2012**, *116*, 12415.
180. Nascimento, L. L.; Brussasco, J. G.; Garcia, I. A.; Paula, L. F.; Polo, A. S.; Patrocinio, A. O. T.; *J. Phys.: Condens. Matter* **2020**, *33*, 055002.
181. Veiga, E. T.; Fernandes, S. L.; Graeff, C. F. O.; Polo, A. S.; *Sol. Energy* **2021**, *214*, 510.
182. Moia, D.; Szumska, A.; Vaissier, V.; Planells, M.; Robertson, N.; O'Regan, B. C.; Nelson, J.; Barnes, P. R. F.; *J. Am. Chem. Soc.* **2016**, *138*, 13197.

183. DiMarco, B. N.; Motley, T. C.; Balok, R. S.; Li, G.; Siegler, M. A.; O'Donnell, R. M.; Hu, K.; Meyer, G. J.; *J. Phys. Chem. C* **2016**, *120*, 14226.
184. Sampaio, R. N.; DiMarco, B. N.; Meyer, G. J.; *ACS Energy Lett.* **2017**, *2*, 2402.
185. Moser, J. E.; Grätzel, M.; *Chem. Phys.* **1993**, *176*, 493.
186. Concepcion, J. J.; House, R. L.; Papanikolas, J. M.; Meyer, T. J.; *Proc. Natl. Acad. Sci. U. S. A.* **2012**, *109*, 15560.
187. Song, W.; Chen, Z.; Glasson, C. R. K.; Hanson, K.; Luo, H.; Norris, M. R.; Ashford, D. L.; Concepcion, J. J.; Brennaman, M. K.; Meyer, T. J.; *ChemPhysChem* **2012**, *13*, 2882.
188. Hammarström, L.; *Acc. Chem. Res.* **2015**, *48*, 840.
189. Xu, P.; McCool, N. S.; Mallouk, T. E.; *Nano Today* **2017**, *14*, 42.
190. Matias, T. A.; Rein, F. N.; Rocha, R. C.; Formiga, A. L. B.; Toma, H. E.; Araki, K.; *Dalton Trans.* **2019**, *48*, 3009.
191. Nunes, B. N.; Bahnemann, D. W.; Patrocinio, A. O. T.; *ACS Appl. Energy Mater.* **2021**, *4*, 3681.
192. Wang, D.; Eberhart, M. S.; Sheridan, M. V.; Hu, K.; Sherman, B. D.; Nayak, A.; Wang, Y.; Marquard, S. L.; Dares, C. J.; Meyer, T. J.; *Proc. Natl. Acad. Sci. U. S. A.* **2018**, *115*, 8523.
193. Purnama, I.; Kubo, Y.; Mulyana, J. Y.; *Inorg. Chim. Acta* **2018**, *471*, 467.
194. Swierk, J. R.; Méndez-Hernández, D. D.; McCool, N. S.; Liddell, P.; Terazono, Y.; Pahk, I.; Tomlin, J. J.; Oster, N. V.; Moore, T. A.; Moore, A. L.; Gust, D.; Mallouk, T. E.; *Proc. Natl. Acad. Sci. U. S. A.* **2015**, *112*, 1681.
195. Ashford, D. L.; Song, W.; Concepcion, J. J.; Glasson, C. R. K.; Brennaman, M. K.; Norris, M. R.; Fang, Z.; Templeton, J. L.; Meyer, T. J.; *J. Am. Chem. Soc.* **2012**, *134*, 19189.
196. Kanan, M. W.; Nocera, D. G.; *Science* **2008**, *321*, 1072.
197. Souza, S. S.; Patrocinio, A. O. T.; *Quim. Nova* **2014**, *37*, 886.
198. Wang, Z. Y.; Zhou, W.; Wang, X.; Zhang, X. L.; Chen, H. Y.; Hu, H. L.; Liu, L. Q.; Ye, J. H.; Wang, D. F.; *Catalysts* **2020**, *10*, 11.
199. Huang, P. P.; Pantovich, S. A.; Okolie, N. O.; Deskins, N. A.; Li, G. H.; *ChemPhotoChem* **2020**, *4*, 420.
200. Zhong, Y. H.; Lei, Y.; Huang, J. F.; Xiao, L. M.; Chen, X. L.; Luo, T.; Qin, S.; Guo, J.; Liu, J. M.; *J. Mater. Chem. A* **2020**, *8*, 8883.
201. Kurarnochi, Y.; Fujisawa, Y.; Satake, A.; *J. Am. Chem. Soc.* **2020**, *142*, 705.
202. Cancelliere, A. M.; Puntoriero, F.; Serroni, S.; Campagna, S.; Tamaki, Y.; Saito, D.; Ishitani, O.; *Chem. Sci.* **2020**, *11*, 1556.
203. Song, W.; Ito, A.; Binstead, R. A.; Hanson, K.; Luo, H.; Brennaman, M. K.; Concepcion, J. J.; Meyer, T. J.; *J. Am. Chem. Soc.* **2013**, *135*, 11587.
204. Sundin, E.; Abrahamsson, M.; *Chem. Commun.* **2018**, *54*, 5289.
205. Li, S.; Li, Z.-J.; Yu, H.; Sytu, M. R.; Wang, Y.; Beeri, D.; Zheng, W.; Sherman, B. D.; Yoo, C. G.; Leem, G.; *ACS Energy Lett.* **2020**, *5*, 777.
206. Badgurjar, D.; Shan, B.; Nayak, A.; Wu, L.; Chitta, R.; Meyer, T. J.; *ACS Appl. Mater. Interfaces* **2020**, *12*, 7768.
207. Song, W. J.; Vannucci, A. K.; Farnum, B. H.; Lapides, A. M.; Brennaman, M. K.; Kalanyan, B.; Alibabaei, L.; Concepcion, J. J.; Losego, M. D.; Parsons, G. N.; Meyer, T. J.; *J. Am. Chem. Soc.* **2014**, *136*, 9773.
208. Bruggeman, D. F.; Bakker, T. M. A.; Mathew, S.; Reek, J. N. H.; *Chem. - Eur. J.* **2021**, *27*, 218.
209. Swierk, J. R.; McCool, N. S.; Mallouk, T. E.; *J. Phys. Chem. C* **2015**, *119*, 13858.
210. Brady, M. D.; Troian-Gautier, L.; Sampaio, R. N.; Motley, T. C.; Meyer, G. J.; *ACS Appl. Mater. Interfaces* **2018**, *10*, 31312.
211. Hanson, K.; Brennaman, M. K.; Ito, A.; Luo, H.; Song, W.; Parker, K. A.; Ghosh, R.; Norris, M. R.; Glasson, C. R. K.; Concepcion, J. J.; Lopez, R.; Meyer, T. J.; *J. Phys. Chem. C* **2012**, *116*, 14837.
212. Karlsson, S.; Boixel, J.; Pellegrin, Y.; Blart, E.; Becker, H.-C.; Odobel, F.; Hammarström, L.; *J. Am. Chem. Soc.* **2010**, *132*, 17977.
213. Song, W.; Glasson, C. R. K.; Luo, H.; Hanson, K.; Brennaman, M. K.; Concepcion, J. J.; Meyer, T. J.; *J. Phys. Chem. Lett.* **2011**, *2*, 1808.
214. Swierk, J. R.; McCool, N. S.; Saunders, T. P.; Barber, G. D.; Mallouk, T. E.; *J. Am. Chem. Soc.* **2014**, *136*, 10974.
215. Kuss-Petermann, M.; Orazietti, M.; Neuburger, M.; Hamm, P.; Wenger, O. S.; *J. Am. Chem. Soc.* **2017**, *139*, 5225.
216. Chen, J.; Kuss-Petermann, M.; Wenger, O. S.; *J. Phys. Chem. B* **2015**, *119*, 2263.
217. Xu, P.; Mallouk, T. E.; *J. Phys. Chem. C* **2019**, *123*, 299.
218. Lyon, L. A.; Hupp, J. T.; *J. Phys. Chem. B* **1999**, *103*, 4623.
219. Halverson, A. F.; Zhu, K.; Erslev, P. T.; Kim, J. Y.; Neale, N. R.; Frank, A. J.; *Nano Lett.* **2012**, *12*, 2112.
220. Ashford, D. L.; Gish, M. K.; Vannucci, A. K.; Brennaman, M. K.; Templeton, J. L.; Papanikolas, J. M.; Meyer, T. J.; *Chem. Rev.* **2015**, *115*, 13006.
221. Ji, Z.; He, M.; Huang, Z.; Ozkan, U.; Wu, Y.; *J. Am. Chem. Soc.* **2013**, *135*, 11696.
222. Sun, J.; Yu, Y.; Curtze, A. E.; Liang, X.; Wu, Y.; *Chem. Sci.* **2019**, *10*, 5519.
223. Nikolaou, V.; Charisiadis, A.; Charalambidis, G.; Coutsolelos, A. G.; Odobel, F.; *J. Mater. Chem. A* **2017**, *5*, 21077.
224. Gatty, M. G.; Pullen, S.; Sheibani, E.; Tian, H.; Ott, S.; Hammarström, L.; *Chem. Sci.* **2018**, *9*, 4983.
225. Pazoki, M.; Cappel, U. B.; Johansson, E. M. J.; Hagfeldt, A.; Boschloo, G.; *Energy Environ. Sci.* **2017**, *10*, 672.
226. Berera, R.; van Grondelle, R.; Kennis, J. T. M.; *Photosynth. Res.* **2009**, *101*, 105.
227. Wang, Y.; Asbury, J. B.; Lian, T.; *J. Phys. Chem. A* **2000**, *104*, 4291.
228. Ardo, S.; Sun, Y.; Staniszewski, A.; Castellano, F. N.; Meyer, G. J.; *J. Am. Chem. Soc.* **2010**, *132*, 6696.
229. Ardo, S.; Sun, Y.; Castellano, F. N.; Meyer, G. J.; *J. Phys. Chem. B* **2010**, *114*, 14596.

230. Pazoki, M.; Hagfeldt, A.; Boschloo, G.; *Electrochim. Acta* **2015**, *179*, 174.
231. George, M. W.; Portius, P. In *Comprehensive Organometallic Chemistry III*; Mingos, D. M. P.; Crabtree, R. H., eds.; Elsevier: Oxford, UK, 2007.
232. Mezzetti, A.; Leibl, W.; *Photosynth. Res.* **2017**, *131*, 121.
233. Kuimova, M. K.; Alsindi, W. Z.; Dyer, J.; Grills, D. C.; Jina, O. S.; Matousek, P.; Parker, A. W.; Portius, P.; Zhong Sun, X.; Towrie, M.; Wilson, C.; Yang, J.; George, M. W.; *Dalton Trans.* **2003**, 3996.
234. Groot, M. L.; van Grondelle, R. In *Biophysical Techniques in Photosynthesis*; Aartsma, T. J.; Matysik, J., eds.; Springer Netherlands: Dordrecht, Netherlands, 2008.
235. Reynal, A.; Forneli, A.; Martinez-Ferrero, E.; Sánchez-Díaz, A.; Vidal-Ferran, A.; O'Regan, B. C.; Palomares, E.; *J. Am. Chem. Soc.* **2008**, *130*, 13558.
236. DiMarco, B. N.; Troian-Gautier, L.; Sampaio, R. N.; Meyer, G. J.; *Chem. Sci.* **2018**, *9*, 940.
237. Wang, D.; Sampaio, R. N.; Troian-Gautier, L.; Marquard, S. L.; Farnum, B. H.; Sherman, B. D.; Sheridan, M. V.; Dares, C. J.; Meyer, G. J.; Meyer, T. J.; *J. Am. Chem. Soc.* **2019**, *141*, 7926.
238. Lee, K. J.; Elgrishi, N.; Kandemir, B.; Dempsey, J. L.; *Nat. Rev. Chem.* **2017**, *1*, 14.
239. Benkö, G.; Kallioinen, J.; Korppi-Tommola, J. E. I.; Yartsev, A. P.; Sundström, V.; *J. Am. Chem. Soc.* **2002**, *124*, 489.
240. Cherepy, N. J.; Smestad, G. P.; Grätzel, M.; Zhang, J. Z.; *J. Phys. Chem. B* **1997**, *101*, 9342.
241. Antila, L. J.; Myllyperkiö, P.; Mustalahti, S.; Lehtivuori, H.; Korppi-Tommola, J.; *J. Phys. Chem. C* **2014**, *118*, 7772.
242. Kallioinen, J.; Benkö, G.; Sundström, V.; Korppi-Tommola, J. E. I.; Yartsev, A. P.; *J. Phys. Chem. B* **2002**, *106*, 4396.
243. Bettis, S. E.; Hanson, K.; Wang, L.; Gish, M. K.; Concepcion, J. J.; Fang, Z.; Meyer, T. J.; Papanikolas, J. M.; *J. Phys. Chem. A* **2014**, *118*, 10301.
244. Ghosh, H. N.; Asbury, J. B.; Lian, T.; *J. Phys. Chem. B* **1998**, *102*, 6482.
245. Asbury, J. B.; Hao, E.; Wang, Y.; Lian, T.; *J. Phys. Chem. B* **2000**, *104*, 11957.
246. Dereka, B.; Koch, M.; Vauthey, E.; *Acc. Chem. Res.* **2017**, *50*, 426.
247. Paz, Y.; *J. Phys.: Condens. Matter* **2019**, *31*, 22.
248. Heimer, T. A.; Heilweil, E. J.; *J. Phys. Chem. B* **1997**, *101*, 10990.
249. Takeshita, K.; Sasaki, Y.; Kobashi, M.; Tanaka, Y.; Maeda, S.; Yamakata, A.; Ishibashi, T.; Onishi, H.; *J. Phys. Chem. B* **2004**, *108*, 2963.
250. Yin, X.; Zhao, H.; Chen, L.; Tan, W.; Zhang, J.; Weng, Y.; Shuai, Z.; Xiao, X.; Zhou, X.; Li, X.; Lin, Y.; *Surf. Interface Anal.* **2007**, *39*, 809.
251. Black, F. A.; Clark, C. A.; Summers, G. H.; Clark, I. P.; Towrie, M.; Penfold, T.; George, M. W.; Gibson, E. A.; *Phys. Chem. Chem. Phys.* **2017**, *19*, 7877.
252. Bisquert, J.; Fabregat-Santiago, F. In *Dye-Sensitized Solar Cells*, 1st ed.; Kalyanasundaram, K., ed.; EPFL Press: Lausanne, Switzerland, 2010.
253. Sarker, S.; Ahammad, A. J. S.; Seo, H. W.; Kim, D. M.; *Int. J. Photoenergy* **2014**, *2014*, 851705.
254. Fabregat-Santiago, F.; Garcia-Belmonte, G.; Bisquert, J.; Zaban, A.; Salvador, P.; *J. Phys. Chem. B* **2002**, *106*, 334.
255. Bisquert, J.; *J. Phys. Chem. B* **2002**, *106*, 325.
256. Baram, N.; Ein-Eli, Y.; *J. Phys. Chem. C* **2010**, *114*, 9781.
257. Fabregat-Santiago, F.; Garcia-Belmonte, G.; Mora-Seró, I.; Bisquert, J.; *Phys. Chem. Chem. Phys.* **2011**, *13*, 9083.
258. Sacco, A.; *Renewable Sustainable Energy Rev.* **2017**, *79*, 814.
259. Lopez-Varo, P.; Jimenez-Tejada, J. A.; Garcia-Rosell, M.; Ravishankar, S.; Garcia-Belmonte, G.; Bisquert, J.; Almora, O.; *Adv. Energy Mater.* **2018**, *8*, 36.
260. Peter, L. M.; Wijayantha, K. G. U.; *Electrochem. Commun.* **1999**, *1*, 576.
261. Dloczik, L.; Ileperuma, O.; Lauermann, I.; Peter, L. M.; Ponomarev, E. A.; Redmond, G.; Shaw, N. J.; Uhlendorf, I.; *J. Phys. Chem. B* **1997**, *101*, 10281.
262. Cao, F.; Oskam, G.; Meyer, G. J.; Searson, P. C.; *J. Phys. Chem.* **1996**, *100*, 17021.
263. Cen, J. J.; Wu, Q. Y.; Liu, M. Z.; Orlov, A.; *Green Energy Environ.* **2017**, *2*, 100.
264. Ravishankar, S.; Riquelme, A.; Sarkar, S. K.; Garcia-Batlle, M.; Garcia-Belmonte, G.; Bisquert, J.; *J. Phys. Chem. C* **2019**, *123*, 24995.
265. Halme, J.; *Phys. Chem. Chem. Phys.* **2011**, *13*, 12435.
266. Kern, R.; Sastrawan, R.; Ferber, J.; Stangl, R.; Luther, J.; *Electrochim. Acta* **2002**, *47*, 4213.
267. Bay, L.; West, K.; *Sol. Energy Mater. Sol. Cells* **2005**, *87*, 613.
268. van de Lagemaat, J.; Park, N. G.; Frank, A. J.; *J. Phys. Chem. B* **2000**, *104*, 2044.
269. Wang, H.; Peter, L. M.; *J. Phys. Chem. C* **2009**, *113*, 18125.
270. von Hauff, E.; *J. Phys. Chem. C* **2019**, *123*, 11329.
271. Parussulo, A. L. A.; Matias, T. A.; Guimaraes, R. R.; Toma, S. H.; Araki, K.; Toma, H. E.; *Inorg. Chim. Acta* **2016**, *453*, 764.
272. Fabregat-Santiago, F.; Bisquert, J.; Palomares, E.; Otero, L.; Kuang, D.; Zakeeruddin, S. M.; Grätzel, M.; *J. Phys. Chem. C* **2007**, *111*, 6550.
273. Fabregat-Santiago, F.; Bisquert, J.; Garcia-Belmonte, G.; Boschloo, G.; Hagfeldt, A.; *Sol. Energy Mater. Sol. Cells* **2005**, *87*, 117.
274. Nakade, S.; Kanzaki, T.; Wada, Y.; Yanagida, S.; *Langmuir* **2005**, *21*, 10803.
275. Adachi, M.; Sakamoto, M.; Jiu, J.; Ogata, Y.; Isoda, S.; *J. Phys. Chem. B* **2006**, *110*, 13872.

276. Wang, Z. S.; Cui, Y.; Dan-oh, Y.; Kasada, C.; Shinpo, A.; Hara, K.; *J. Phys. Chem. C* **2007**, *111*, 7224.
277. Zhu, Y.; Wang, D.; Huang, Q.; Du, J.; Sun, L.; Li, F.; Meyer, T. J.; *Nat. Commun.* **2020**, *11*, 4610.
278. Neukom, M.; Zufle, S.; Jenatsch, S.; Ruhstaller, B.; *Sci. Technol. Adv. Mater.* **2018**, *19*, 291.
279. Huo, Z.; Tao, L.; Wang, L.; Zhu, J.; Chen, S.; Zhang, C.; Dai, S.; Zhang, B.; *Electrochim. Acta* **2015**, *168*, 313.
280. James, E. M.; Bennett, M. T.; Bangle, R. E.; Meyer, G. J.; *Langmuir* **2019**, *35*, 12694.
281. Barr, T. J.; Meyer, G. J.; *ACS Energy Lett.* **2017**, *2*, 2335.
282. Wang, X.; Karanjit, S.; Zhang, L.; Fong, H.; Qiao, Q.; Zhu, Z.; *Appl. Phys. Lett.* **2011**, *98*, 082114.
283. Barnes, P. R. F.; Miettunen, K.; Li, X.; Anderson, A. Y.; Bessho, T.; Gratzel, M.; O'Regan, B. C.; *Adv. Mater.* **2013**, *25*, 1881.
284. Boschloo, G.; Häggman, L.; Hagfeldt, A.; *J. Phys. Chem. B* **2006**, *110*, 13144.
285. Barr, T. J.: *Interfacial Electron Transfer at Sensitized Nanocrystalline TiO_2 Electrolyte Interfaces: Influence of Surface Electric Fields and Lewis-Acidic Cations*; PhD thesis, University of North Carolina at Chapel Hill, North Carolina, United States, 2017, available at https://cdr.lib.unc.edu/concern/dissertations/pc289k26z, accessed in May 2021.
286. DiMarco, B. N.; O'Donnell, R. M.; Meyer, G. J.; *J. Phys. Chem. C* **2015**, *119*, 21599.
287. Brady, M. D.; Troian-Gautier, L.; Motley, T. C.; Turlington, M. D.; Meyer, G. J.; *ACS Appl. Mater. Interfaces* **2019**, *11*, 27453.
288. Blauch, D. N.; Saveant, J. M.; *J. Am. Chem. Soc.* **1992**, *114*, 3323.
289. Qu, P.; Meyer, G. J.; *Langmuir* **2001**, *17*, 6720.

Submitted: March 8, 2021
Published online: June 8, 2021